UNIVERSIDAD SAN FRANCISCO DE QUITO USFQ

Colegio de Ciencias e Ingenierías

Detection of Spin Wave Beam in Magnetostatic Forward Volume Waves

Proyecto de investigación

Nicolás Agenor Loayza Romero

Licenciatura en Física

Trabajo de titulación presentado como requisito
para la obtención del título de Licenciado en Física

Quito, 9 de diciembre de 2016

UNIVERSIDAD SAN FRANCISCO DE QUITO USFQ

COLEGIO DE CIENCIAS E INGENIERÍAS

HOJA DE CALIFICACIÓN

DE TRABAJO DE TITULACIÓN

Detection of Spin Wave Beam in Magnetostatic Forward Volume Waves

Nicolás Agenor Loayza Romero

Calificación:

Nombre del profesor: Vincent Vlaminck Ph.D.

Firma del profesor: _____

Quito, 9 de diciembre de 2016

DERECHOS DE AUTOR

Por medio del presente documento certifico que he leído todas las Políticas y Manuales de la Universidad San Francisco de Quito USFQ, incluyendo la Política de Propiedad Intelectual USFQ, y estoy de acuerdo con su contenido, por lo que los derechos de propiedad intelectual del presente trabajo quedan sujetos a lo dispuesto en esas Políticas.

Asimismo, autorizo a la USFQ para que realice la digitalización y publicación de este trabajo en el repositorio virtual, de conformidad a lo dispuesto en el Art. 144 de la Ley Orgánica de Educación Superior.

Firma del estudiante: _____

Nombres y apellidos: Nicolás Agenor Loayza Romero

Código: 00113310

Cédula de identidad: 171805444-6

Lugar y fecha: Quito, 9 de diciembre de 2016

A mi familia, Tamia y amigos.

Agradecimientos

*Agradezco a USFQ y a "Agence Nationale de la Recherche" por la ayuda económica, mediante beca "*Investissments d'avenir*" código: ANR-11-LABX-0058_NIE.*
Al Dr. Matthieu Bailleul por su ayuda para este proyecto.
A la gente que trabaja para la plataforma de nanofabricación STnano del Instituto de Física y Química de los Materiales de Estrasburgo (IPCMS), Francia.
A Argonne National Laboratory por proveernos de las películas continuas de YIG.
A todo aquel que, de alguna u otra manera, me ha brindado su apoyo para que pueda culminar mi carrera.
A mi familia por apoyarme y alentarme en todo momento.
A Tamia por soportar días de Tesis y exámenes, y aún así seguir aquí conmigo.
A mis profesores por ser guías y amigos.
En especial a Vincent Vlaminck por ser de quién más he aprendido y quién más me apoyo.
Por último a mis amigos, los físicos, que hicieron estos cuatro años memorables.
Barcelona Campeón!!!

Resumen

Magnónica es un campo de investigación reciente el cual empezó en la última década. Recientes desarrollos de nuevos materiales y técnicas experimentales abren oportunidades para dispositivos basados en ondas de espín. En analogía con la importancia de el láser en el campo de la fotónica, la excitación de un haz de ondas de espín en películas magnéticas continuas está aún por evidenciarse. En este trabajo se presenta el estudio experimental de distintas geometrías de antenas de tamaño micrométrico para evidenciar por primera vez la emisión de un haz de ondas de espín. Se procedió a un mapeo discreto de la amplitud de las ondas de espín en películas continuas del material ferromagnético YIG ($Y_3Fe_2(FeO_4)_3$), usando varios pares de guías de onda coplanares con pequeñas constricciones, vía espectroscopía de ondas de espín. Usando el espectro de las ondas de espín, observamos que la propagación de ondas magntostáticas volumétricas hacia adelante están relativamente confinadas en un haz de tamaño comparabable al de la constricción.

Palabras clave: Haz de Ondas de Espín, YIG, Resonancia Ferromagnética, Ondas Magnetostáicas.

Abstract

Magnonics is a new field of research which started in the last decade. Recent development of new materials and experimental techniques opened up opportunities for devices based on spin waves. In analogy with the importance of a laser in the field of photonics, the excitation of a spin wave beam in continuous magnetic layers is yet to be evidence. This work presents the experimental study of different geometries of sub-micrometer size antennae to evidence for the first time the emission of a spin wave beam in a continuous layer. We proceed to a discrete mapping of the spin wave amplitude in thin films of YIG (Yttrium-Iron Garnet, ($Y_3Fe_2(FeO_4)_3$) using several pairs of coplanar wave guides with small constrictions via spin wave spectroscopy. Using the spin wave spectra, we observed that the propagation of magnetostatic forward volume waves are relatively confined within a beam of size comparable to the constriction.

Key words: Spin Wave Beam, YIG, Ferromagnetic Resonance, Magnetostaic Waves.

Index

1 Introduction **14**

2 Magnetostatics **17**
2.1 Types of Magnetic Materials 19
2.2 Ferromagnetism 20
2.3 Magnetic Interactions and magnetic energies 21
2.3.1 Exchange Interaction 21
2.3.2 Zeeman Energy 22
2.3.3 Demagnetizing energy 22
2.3.4 Cubic Anisotropy Energy 23
2.3.5 Uniaxial Anisotropy Energy 23
2.4 Effective Fiedl $\mathbf{H}_{eff}$ 24

3 Magnetization Dynamics: Uniform excitation **25**
3.1 Landau - Lifshitz equation 25
3.2 Linearization of Lifshitz-Landau equation 25
3.3 Gilbert Damping 26
3.4 Dynamic Susceptibility Tensor for Thin film with out of plane External field . . 26

4 Spin Waves: Non-Uniform excitation **30**
4.1 Electromagnetic waves in Anisotropic Media 30
4.2 Magnetostatic Approximation 31
4.3 Walker's Equation 32
4.4 Normally magnetized film 33
4.5 Tangentially magnetized film: Backward Volume Waves 35
4.6 Tangentially magnetized film: Surface Waves 36

5 Experimental Techniques **37**
5.1 Ferromagnetic Resonance 37
5.1.1 Lock in Amplification with Amplitude Modulation 38
5.1.2 Ferromagnetic Resonance in thin films via Vector Network Analyzer detection 41
5.1.3 Vector Network Analyzer 41
5.1.4 FMR characterization via VNA detection 43
5.2 Propagating Spin Wave Spectroscopy (PSWS) 47

6 Antennae Design **50**
6.1 Fresnel Diffraction 50

6.2 Fabricated Antennae 52

7 Fabrication Process **55**
7.1 Electron Beam Lithography 55
7.1.1 Mask Pattern 55
7.1.2 Lithography 55
7.2 Metal Deposition 56

8 Results **58**
8.1 Attenuation Length 58
8.2 Focusing: same size shifted antennae 62
8.3 Mapping 63
8.4 Sudden constriction geometries 67

9 Conclusions **69**

Appendices **71**

10 References **78**

Figure Index

1 a) plot of phase of the spin wave vs. current I b) Geometry of the setup b) Signal outputs for the given inputs. [15] 14

2 a) Geometry of the CPW that excites spin waves and the two media determined by the thickness. b) Refraction of the spin wave when it passes from one media to another. [10] 15

3 Deviation of spin wave snell's law from opctical snell's law a) in refraction b) in reflection.[10] 15

4 a) Geometry of the CPW to excite spin wave beam. b) Mapping of the magnetization in the x-y plane, with out of plane external field. c) mapping of the excitation field showing the constriction in the center of the CPW. [8] 16

5 Magnetic dipole showing the field lines of the magnetic field. 17

6 Sketch of Paulli paramagnetism a) When $\mathbf{H}_{ext} = 0$ the spins up and down coexist with the same fermi energy. b) and c) When $\mathbf{H}_{ext} \neq 0$ the fermi level splits into two sides with an increase of energy (spin up) and the other with a decrease of energy (spin down). 20

7 Free energy close to the critical temperature. For $T < T_c$ there is minimum value at $(\pm M_s)$, for $T > T_c$ minimum is at $M = 0$ paramagnetic state 21

8 Skecth of magnetic interactions, a) Exchange interaction b) Demagnetizing field c) Anisotropy field 24

9 Sketch of a) the precession of $\mathbf{M}$ around $\mathbf{H}_{eff}$. b) Sketch shows the additional term that points toward $\mathbf{H}_{eff}$[1] 26

10 Real and imaginary part of the term χ_{yy} of the susceptibility tensor. Imaginary part has a Lorentzian lineshape, and is the responsible of the damping of the precession. Real part is the derivative of a Lorentzian. 29

11 Thin film of ferromagnetic material magnetized along z-axis. A wave in the film can be analyzed as planes waves bouncing between the surfaces of the film, which can be seen as standing waves along the thickness. 33

12 Thin film of ferromagnetic material magnetized along x-axis. Wave modes depend od the relative direction of the $\mathbf{k}$ vector. a) $\mathbf{H}_{ext} \parallel \mathbf{k}$ the mode is Backward volume waves. b) $\mathbf{H}_{ext} \perp \mathbf{k}$ the mode is Surface waves 36

13 a) Coplanar Waveguide, the current trough creates the small oscillating field necessary to induce Resonance. b) Normalized Fourier transform of the current density in a single CPW line with $w = 400nm$ and $s = 200nm$ 38

14 a) Set up of the FMR station using diode detection, lock-in amplification and amplitude modulation of the microwave signal. b) Picture of the CPW with a thin film of permalloy. c) Picture, showing the electromagnet and the rack for the generator and lock-in amplifier, of FMR set up in the Laboratory of Solid State Physics at USFQ. 39
15 Spectra of power absorption of microwave signal due to ferromagnetic resonance of YIG thin films. a) $f_{res} = 3.25\,GHz$ b) $f_{res} = 5.75\,GHz$ 40
16 Spectra of power absorption of microwave signal due to ferromagnetic resonance. a) Fitting of Kittel's formula for in plane field in thin films FMR. b) Determination of the damping coefficient(α) from the linewidth of the resonance curve. 41
17 Schemme of a DUT showing the ongoing and outgoing waves in each port, credits: [1]. 42
18 Picture of FMR setup in Laboratory of Magnetic Susceptibilities at IPCMS. . . 43
19 a) Top view of film with CPW used to perform FMR for uniform excitation. Spectra in reflection ΔL_{11} b) $\mu_o H_{ext} = 0,3507 \quad T$ b) $\mu_o H_{ext} = 0,4073 \quad T$. c) $\mu_o H_{ext} = 0,6934 \quad T$ 44
20 Spectra in reflection ΔL_{11}. This spectra correspond for non-uniform excitation for a CPW with $k_2 = 5.9\mu m^{-1}$. a) $\mu_o H_{ext} = 0.3507 \quad [T]$. b) $\mu_o H_{ext} = 0.4073 \quad [T]$ c) $\mu_o H_{ext} = 0.6123 \quad [T]$ 46
21 Fitting of Kittel formula to extract H_k, γ and M_s. a) Resonance frequency as function of external field, for $k = 0$ and $k_2 = 5.9\mu m^{-1}$. b) Difference of the square of the frequency of resonance. 47
22 Pair of antennae for PSWS technique. a) Optical picture showing the direction of the current in th signal and ground lines. b) SEM picture of pair of antenna showing the dimensions of importance for the characterization of the spectra. c) Amplitude square of the current normalized Fourier Transform of the current density for the antenna, just the constriction. 48
23 a) spectra in reflection and transmission, ΔL_{11} and $\Delta L12$. b) Spectra in transmission, the f_{osc} is the frequency difference of two adjacent peaks. c) dispersion relation for MFVW's with $\mu_o H_{eff} = 0.2T$ and $\mu_o M_s = 0.15T$, d) Fourier transform of a CPW for $\lambda = 1\mu m$ 49
24 Geometry of an antennae emitting spherical waves to measure the intensity at a perpendicular plane to the antenna at distance D. 50
25 Amplitude profile of an spin wave measured at distinct distances, a) $\lambda = 1\mu m$, $L_{att} = 7\,\mu m$ and $w = 5\mu m$ b) $\lambda = 1\mu m$, $L_{att} = 7\,\mu m$ and $w = 5\mu m$, averaging with the probe size $w = 2\,\mu m$ 51

26 Amplitude profile of an spin wave measured at distinct distances, a) $\lambda = 1\mu m$, $L_{att} = 7\ \mu m$ and $w = 10\mu m$ b) $\lambda = 1\mu m$, $L_{att} = 7\ \mu m$ and $w = 10\mu m$, averaging with the probe size $w = 2\ \mu m$ 51
27 a) Optical image of developed film after lithography of antenna with continuous constriction, Geometry No. 1. $w = 5\mu m$, $\lambda = 1\mu m$, $D = 4\mu m$ b) SEM image of device of antenna with sudden extreme bend and end shorted, Geometry No. 2. $w5\mu m$, $\lambda = 1\mu m$, $D = 4\mu m$, Mapping device shift $s = -4\mu m$ 52
28 a) SEM image of antenna with sudden constriction, Geometry No. 3. $w = 5\mu m$, $\lambda = 1\mu m$, $D = 4\mu m$ b) SEM image of the device of antenna with sudden constriction and end shorted, Geometry No. 4. $w = 10\mu m$, $\lambda = 1.2\mu m$, $D = 8\mu m$ 52
29 FMR device. SEM image of the device, $w = 20\mu m$, $\lambda = 1\mu m$ 53
30 a) Optical image of developed film after lithography of antenna with continuous constriction, Geometry No. 1. Mapping device, Receiver shifted $5 = \mu m.$, constriction length of emitter $10\mu m$, width of receiver $w = 2\mu m$, $\lambda = 1.2\mu m$, $D = 5\mu m$ b) Optical image of developed film after lithography of Antenna with continuous constriction, Geometry No. 1. same length constriction, shifted one respect to other. Receiver shifted $5 = \mu m$, constriction width $5\mu m$, $\lambda = 1\mu m$, $D = 4\mu m$ 53
31 Summary of all devices fabricated, working devices (✓), no working devices (x) 54
32 Mask for antenna, Distance $4\mu m$, Width of antenna $1.2\mu m$, length of antenna $5\mu m$. 56
33 Zeiss Supra 40 electron beam microscope at IPCMS. 56
34 a) Plassys MEB550S electron beam evaporator at IPCMS. b) E-beam evaporation process. A beam of electrons is guided with a magnetic field, the beam hits the metal source and evaporates metal which ascends and is deposited on the film. The rate of deposition is controlled with a quartz detector. 57
35 Optical image of developed film after lithography of antenna with continuous constriction, Geometry No. 1. $w = 5\mu m$, $\lambda = 1\mu m$, $D = 14\mu m$. 59
36 Spectra in transmission $|\Delta L_{12}|$, real and imaginary part, Geometry No. 1 $w = 5\mu m$, $\lambda = 1\mu m$ and $D = 4\mu m$. a) $\mu_o H_{ext} = 0,2427T$. b) $\mu_o H_{ext} = 0,3082T$. c) $\mu_o H_{ext} = 0,4073T$ 59
37 Antennae with $\lambda = 1\mu m$ a) $\ln|\Delta L_{12}|$ vs. D, to obtain L_{att} b) f_{osc}^{-1} vs. D, to obtain v_g. c) frequency vs. v_g/L_{att}, to obtain effective Damping. 60
38 Antennae with $\lambda = 2\mu m$ a) $\ln|\Delta L_{12}|$ vs. D, to obtain L_{att} b) f_{osc}^{-1} vs. D, to obtain v_g. c) frequency vs. v_g/L_{att}, to obtain effective Damping. 61
39 Antennae with $\lambda = 1\mu m$, $w = 5\mu m$ and $D = 4\mu m$ a) s=0w b) s=0.5w c) s=1w d) s=1.5w 62

40 Amplitude in transmission $|\Delta L_{12}|$ vs. normalized frequency, for same size antennae shifted, $D = 4\mu m$. a) $\mu_o H_{ext} = 0.2427T$ b) $\mu_o H_{ext} = 0.3082T$ c) $\mu_o H_{ext} = 0.3741T$ 63
41 Amplitude in transmission $|\Delta L_{12}|$ vs. normalized frequency, for same size antennae shifted, $D = 10\mu m$. a) $\mu_o H_{ext} = 0.2427T$ b) $\mu_o H_{ext} = 0.3082T$ c) $\mu_o H_{ext} = 0.3741T$ 63
42 Mapping devices. Emitter $w = 10\mu m$ and Receiver $w = 2\mu m$, both with $\lambda = 1\mu m$ a) $s = 2\mu m$ b) $s = 3\mu m$ 64
43 Spectra in Reflection both ports, and in transmission ΔL_{12} for mapping device with $\mu_o H_{ext} = 0.3741T$ a) $s = 0\mu m$ b) $s = 6\mu m$ 65
44 Mapping of amplitude for Geometry No. 1. black line shows the edge of the constriction. 65
45 Mapping grid for Geometry No. 2. 66
46 Mapping for Geometry No. 2. Black lines show edges of the constriction. . . . 66
47 Spectra in transmission and reflection for Geometry No. 3 a)$\mu_o H_{ext} = 0.2427T$ b) $\mu_o H_{ext} = 0.3741T$ c) $\mu_o H_{ext} = 0.6123T$ d) SEM picture of device with $\lambda = 1\mu m$, $w = 5\mu m$, $D = 8\mu m$ 68
48 Spectra in transmission and reflection for Geometry No. 4 a)$\mu_o H_{ext} = 0.2427T$ b) $\mu_o H_{ext} = 0.3741T$ c) $\mu_o H_{ext} = 0.6123T$ d) SEM picture of device with $\lambda = 1\mu m$, $w = 5\mu m$, $D = 8\mu m$ 68
49 Differential section of a transmission line 71
50 Coaxial transmission line 73
51 Plot of magnetic field in the region between the poles as a function of the coil current. $H_{ext}(I)$ 75
52 Field inhomogeneities of magnetic field as function of the distance to the center of the pole, for $I = 0.5\ A$ 76

1 Introduction

Magnonics is a recent field of research, which developed in the last 10 years, and uses magnetic excitations (e.g. spin waves) for the transmission of information. Several investigations have shown the potential of the use of spin waves, in particular with magnonics based logic gates[14, 15] and magnonic crystals [4]. Spin waves are the precession of the magnetization vector (M) in ferromagnetic materials which propagates away from the excitation device. Magnonic devices present functionalities, which are not currently available in electronics or photonics devices. For example, spin wave dispersion relation is external field dependent, which means the device is easily manipulated by applied magnetic field[12]. Another advantage respect to electronics is that a magnonic devices reduce power consumption, as it is one of the biggest problems of high integrated circuits, because the heating of circuits damage and diminished the lifetime of batteries[4]. Finally, magnonic devices are expected to perform larger number of operations per unit area, than CMOS technology. [13] This is comparing the minimum length feature, gate length for CMOS technology and wavelengths for spin waves, even though current fabrication technology set a limit of hundreds of nanometer for spin waves.

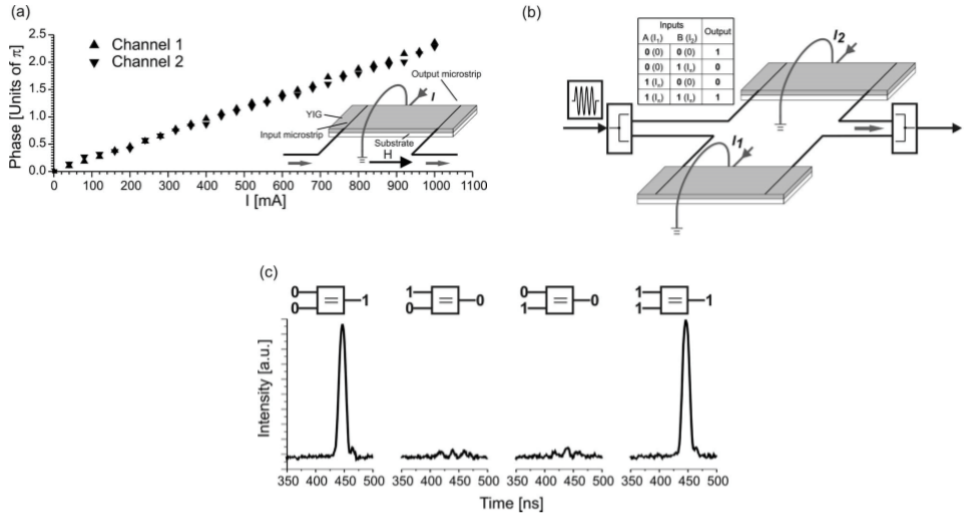

Figure 1: a) plot of phase of the spin wave vs. current I b) Geometry of the setup b) Signal outputs for the given inputs. [15]

Logic gates are devices that can perform logical operations. A logic gate receives two or more logical inputs, 0 or 1, and produces one logical output, 0 or 1, depending on the type of gate. Currently, logic gates are devices based on electronics, but several groups have been working on the implementation of logic gates using spin waves. The realization of XNOR logic gate using magnetic excitations was studied by Schneider et. al [15]. In their experiment (see figure 1) they used two strips of ferromagnetic materials, each arm corresponding to the logical inputs, conductive wire over the strip to create a field which control the dispersion of the spin wave, and a microwave source and detector at each side of the strip. They found that the phase

accumulated ϕ and the current I on each arm have a linear relation. They set that a spin wave with $\phi = 0$ corresponds to the logic value 0, and the spin wave with $\phi = \pi$ corresponds to the logic value 1. Using the conductive wires next to the spin wave strips, they can set the value of the current $I = 0$ that produces $\phi = 0$, and the current I_π that produces $\phi = \pi$, which allows to perform logic operations as shown in figure (1.b)). As the limits of fabrication of logic gates using electronics are reaching their maximum, this work allows possible uses of magnonics for better computational systems.

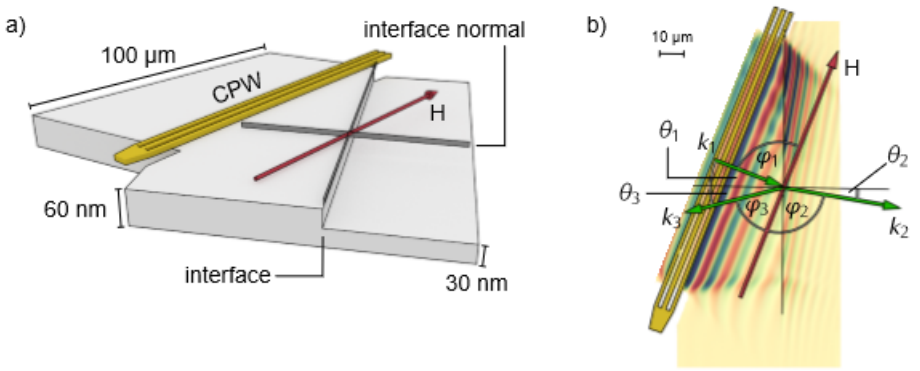

Figure 2: a) Geometry of the CPW that excites spin waves and the two media determined by the thickness. b) Refraction of the spin wave when it passes from one media to another. [10]

More recently, Snell's law in spin waves was studied by Stigloher et.al [10]. They fabricated ferromagnetic films with different thickness, which alters the dispersion relation of spin waves in each region, see figure (2), measured the angle of reflection and refraction for waves that go from one media to another, see figure (3). They found that for angles of incidence greater than $25°$ the refraction angle deviates from optics Snell's law, due to the anisotropic nature of the dispersion relation for spin waves. This work shows the variety of phenomena that spin waves presents and can be useful for future developments in this area.

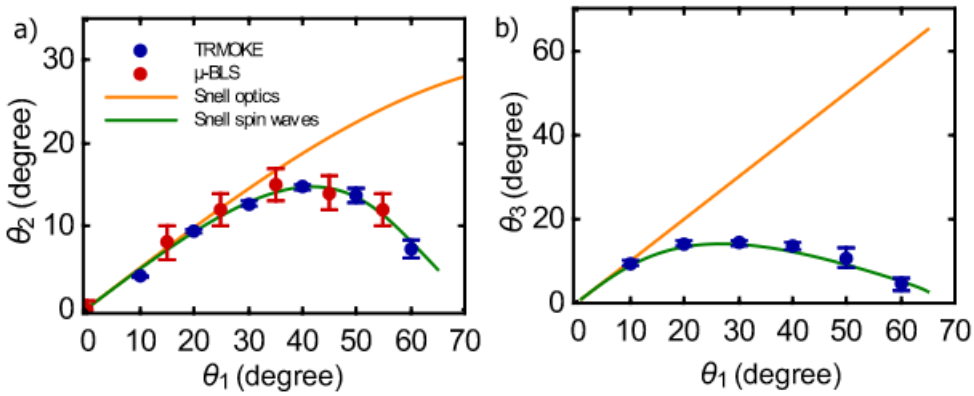

Figure 3: Deviation of spin wave snell's law from opctical snell's law a) in refraction b) in reflection.[10]

The main motivation for this work came from the micromagnetic simulations done by Gruszecki et.al [8]. They found that a Coplanar wave guide (CPW) with a constriction will excite a spin wave beam of a size slightly bigger than the width of the constriction. This is satisfied by the condition that all the resonant peaks from the emission spectrum of the CPW are wellseparated. In figure (4) we can see that for the given geometry the magnetization vector propagates inside a column determined by the constriction.

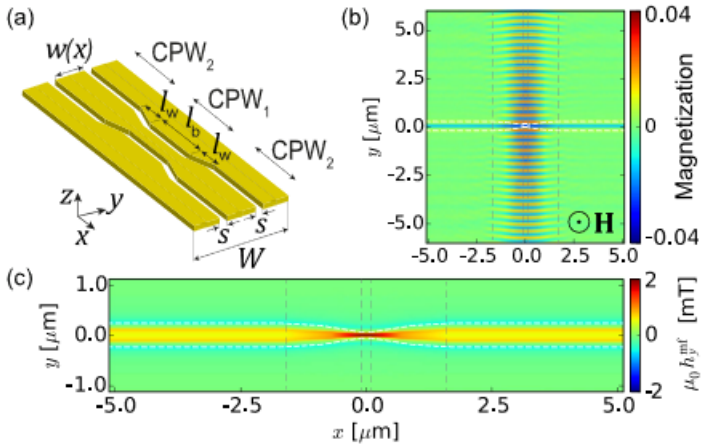

Figure 4: a) Geometry of the CPW to excite spin wave beam. b) Mapping of the magnetization in the x-y plane, with out of plane external field. c) mapping of the excitation field showing the constriction in the center of the CPW. [8]

In a similar manner as the importance of the laser for the advance of photonics, the realization of a spin wave beam in a continuous layer could play a key role for the future of magnonic devices. In this work, we present an experimental study of different geometries for antennae to observe the degree of dispersion of a spin wave beam excited by a constricted CPW in continuous layer of ferromagnetic thin films of YIG. The present thesis is organized as follows. In the second section we present the basics of magnetostatics needed to understand the concept of effective field. In the third section, we present the formalism for uniform excitation in ferromagnetic thin films. In the fourth section, we present the formalism of non-uniform excitations in thin films, e.g. spin waves. In the fifth section, we present experimental techniques used to study magnetization dynamics, and we present results of ferromagnetic resonance, both via diode detection and also via Vector Network Analyzer detection, in YIG thin flims. In this section, we also introduce the technique to excite and detect spin waves called Propagating Spin Wave spectroscopy. In the sixth section, we present spin wave Fresnel diffraction, and the design elements for antennae. In the seventh section, we present the micro-fabrication techniques implemented on the conception of the antennae. In the eighth section, we present spectra of the spin wave transduction that demonstrate the focusing of the spin wave beam. Finally, we summarize all the important results, and an outlook for possible future developments that will bring insightful results.

2 Magnetostatics

Magnetism in materials is from a purely quantum mechanical origin, where the electrons are the one responsible for the macroscopic magnetic order. In a first approach we can think on *classical* magnetic dipoles in a crystalline structure, each dipole generates a magnetic field. The following expression is the field in $\mathbf{r}'$ produced by a magnetic dipole $\mathbf{m}$, located at $\mathbf{r}$:

$$\mathbf{B}(\mathbf{r}') = \frac{\mu_o}{4\pi}\left[\frac{3(\mathbf{m}\cdot(\mathbf{r}'-\mathbf{r})(\mathbf{r}'-\mathbf{r}))}{|\mathbf{r}'-\mathbf{r}|^5} - \frac{\mathbf{m}}{|\mathbf{r}'-\mathbf{r}|^3}\right] \tag{1}$$

If we consider another magnetic dipole at position $\mathbf{r}'$ this experiences a Torque due to $\mathbf{m}$, given by the following expression:

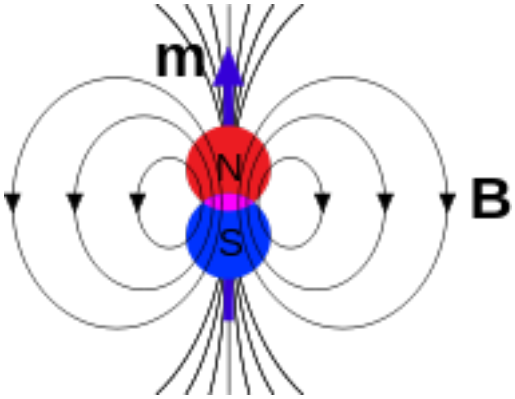

Figure 5: Magnetic dipole showing the field lines of the magnetic field.

$$\tau = \mathbf{m}' \times \mathbf{B}(\mathbf{r}') \tag{2}$$

Then we can write the energy of interaction between two magnetic dipoles:

$$U = -\mathbf{B}\cdot\mathbf{m}' = \frac{\mu_o}{4\pi}\left[\frac{3(\mathbf{m}\cdot(\mathbf{r}'-\mathbf{r}))((\mathbf{r}'-\mathbf{r})\cdot\mathbf{m}')}{|\mathbf{r}'-\mathbf{r}|^5} - \frac{\mathbf{m}\cdot\mathbf{m}'}{|\mathbf{r}'-\mathbf{r}|^3}\right] \tag{3}$$

To obtain the magnetic energy of this material, we sum over all the magnetic dipoles. The dipolar interaction tends to align neighboring dipoles antiparallel, due to the torque, therefore this interaction cannot be the responsible for the magnetic order in ferromagnetic materials.

In the framework of Quantum Mechanics, dynamic variables, like magnetic moments, are considered as operators that acts on wave functions, representing particles. The values that take functions when the operators acts on them are the observables. We define the operator Spin, denoted by $\hat{\mathbf{S}}$, which is the operator for intrinsic angular momenta of each particle. We consider in particular two operators, the projection of $\hat{\mathbf{S}}$ on z-axis $\hat{\mathbf{S_z}}$, and the magnitude square $\hat{\mathbf{S^2}}$. The quantum number s is intrinsic for each particle. The operator $(\hat{S}_z)$ takes the values:

$$\{\hat{\mathbf{S_z}}\} = s, s-1, \ldots, (-s) \tag{4}$$

in particular for the electron is $s = 1/2$, then we have $\{\hat{\mathbf{S}}_\mathbf{z}\} = \pm 1/2$, identified as spin-up and spin down. We set arbitrary to take the projection on the z-axis of $\hat{S}$, in this case projections on x-axis and y-axis are not representative, but the magnitude square is. $\mathbf{S^2}$ takes the values:

$$\{\hat{\mathbf{S}}^\mathbf{2}\} = s(s+1) \tag{5}$$

Considering as well the orbital of the electron an orbital angular momentum is defined $\hat{\mathbf{L}}$ with the same representation as $\hat{\mathbf{S}}$. $\hat{\mathbf{L}}$ is not an intrinsic property an it depends on the orbital position. We define a total angular momentum $\hat{\mathbf{J}} = \hat{\mathbf{S}} + \hat{\mathbf{L}}$. In this sense we define a magnetic moment effecto of the crystal field:

$$\hat{\mathbf{m}} = -\gamma_s \hbar \hat{\mathbf{S}} \tag{6}$$

where $\hbar$ is the reduced planck's constant, and γ_s is the gyromagnetic ratio which is characteristic for each material. More precisely γ_s can be expressed as:

$$\gamma_s = \frac{g|e|}{2m_e} \tag{7}$$

where g is known as the Landé g-factor, for a free electron is $g \approx 2$, e is the charge of the electron, m_e is the mass of the electron. The measured gyromagnetic ratio of a free electron is $\gamma_s = 28.023\, GHz/T$. If the electron is in orbit, we have to add the orbital angular momentum the magnetic dipole is

$$\hat{\mathbf{m}} = -\gamma \hbar \hat{\mathbf{J}} \tag{8}$$

Now γ is a characteristic of the crystal and can be used as characterization parameter. Using Quantum mechanics [3] can be proved that g-factor of an electron in a single atom with the quantum numbers S, L and J is:

$$g_J = \frac{3}{2} + \frac{S(S+1) - L(L+1)}{2J(J+1)} \tag{9}$$

In the rest of the section we will present the variety of magnetic materials and how to characterize them. In magnetism we work with Magnetization, $\mathbf{M}$, which is just the degree at what a body can be magnetized, and its defined as the volume density of magnetic moments:

$$\mathbf{M} = \frac{\sum_{\Delta V} \mathbf{m}}{\Delta V} \tag{10}$$

the units of magnetization are A/m in SI units. Magnetization is also the important quantity that will allow us to understand the dynamics of magnetic materials [3]. We, also, define $\mathbf{H}$ as the external field, while $\mathbf{B}$ as the field of induction or in matter. We can write the following expression to relate them:

$$\mathbf{B} = \mu_o(\mathbf{H} + \mathbf{M}) \tag{11}$$

In free space induction field and H-field are related by the simple equation $\mathbf{B} = \mu_o \mathbf{H}$ [2]. The magnetic response (response of M) to an external field $\mathbf{H}$ can be characterized by the magnetic susceptibility, defined as follows

$$\mathbf{M} = \chi \mathbf{H} \tag{12}$$

susceptibility χ_{ij} can be a symmetric second-rank tensor. Linear magnetic materials presents permeability related with $\mathbf{B}$ and $\mathbf{H}$ fields, as $\mathbf{B} = \mu \mathbf{H}$, using equation (11), we can show that $\mathbf{B} = \mu_o(1 + \chi)\mathbf{H}$, where we identified $\mu_r = 1 + \chi$ as the relative permeability [2].

2.1 Types of Magnetic Materials

We describe here all the types of magnetic materials and its particularities.

- *Diamagnetic Materials*: The magnetic moments of individual atoms and ions, in the absence of field, are randomly distributed, and no net magnetization is present. When a external field is applied, ions organize in direction opposed to external field, susceptibility is negative. The susceptibility is often very-small $\approx 10^{-6}$ [7]. The origin of this effect is due to the electrons in the outer orbitals of the atoms. When an external magnetic field is applied the electrons create a opposite magnetic field, in correspondence with lenz law. This theory is known as Langevin diamagnetism[2]. Diamagnetism is present in all elements, but it is a very small effect.

- *Paramagnetic Materials*: The magnetic moments of individual atoms and ions, in the absence of field, are randomly distributed, and no net magnetization is present. When an external field is applied, ions organize in direction to external field, susceptibility is positive. The susceptibility is often very-small $\approx 10^{-5}$ or 10^{-3} [7]. For some conductors, when a field is applied, the electrons of the Fermi level split into spin-down and spin-up, see figure (6). This phenomena is known as Pauli Paramagnetism it is almost independent of Temperature.

- *Ferromagnetic Materials*: This materials, in the absences of magnetic field, present a spontaneous magnetization below a critical temperature T_c. This means that all magnetic moments, inside a magnetic domain, are aligned to some particular direction. Magnetic domains have an interface between them called domain walls. For temperatures above T_c, a material goes into paramagnetic state. The transition between this two states is a second order phase transition. Ferromagnetic materials are the ones we work with to propagate spin waves.

- *Antiferromagnetic Materials*: Magnetic moments are aligned anti parallel respect neighbors, causing no net magnetization. When a magnetic field is applied, neighbors decrease its angle slightly, causing small and positive susceptibility.

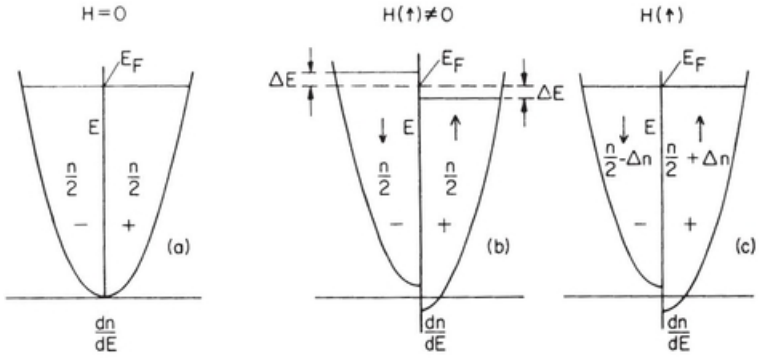

Figure 6: Sketch of Paulli paramagnetism a) When $\mathbf{H}_{ext} = 0$ the spins up and down coexist with the same fermi energy. b) and c) When $\mathbf{H}_{ext} \neq 0$ the fermi level splits into two sides with an increase of energy (spin up) and the other with a decrease of energy (spin down).

- *Ferrimagnetic Materials*: Magnetic domains organized in anti ferromagnetic way, but some discrepancy of direction between domains, produce a net magnetization. Macroscopically is like a ferromagnet, with large and positive susceptibility, but microscopically is like an antiferromagnet.

In this terms, we will focus on Ferromagnets, and its dynamics. We will discuss the origin of ferromagnetism using a phenomenological approach, discussing later all the interactions that allow the magnetic moments to order themselves.

2.2 Ferromagnetism

We will follow a phenomenological approach to understand ferromagnetism, known as Landau theory of ferromagnetism. Assuming there is a magnetic interaction between magnetic moments, that we will discuss further in this section. We suppose that **M** is aligned to the internal total field $\mathbf{H}*$, to be defined later. We can expand the free energy $G(M)$ in even powers of M, because there is no preferred direction in the absence of external field.

$$G(M) = AM^2 + BM^4 + \cdots - \mu_o HM \tag{13}$$

where coefficients A and B are temperature dependent. Here G is the energy of the state when is forced to adopt some value. The value adopted by M should be that it minimizes G, the preferred state. For example, in the ferromagnetic state, M should be $M = \pm M_s$ (M_s saturation magnetization), magnetic moments are oriented in some particular way, there is two minimum in G, therefore $A < 0$ and $B > 0$. If the temperatures rises, and the order is broken, energy minimum is at $M = 0$, so $A < 0$ and $B > 0$. We can see that A should change its sign when temperature pass through some critical value T_c. A is of the form $a(T - T_c)$, where a is a

positive constant. The equilibrium magnetization G minimizes, $\partial G/\partial M = 0$, which implies:

$$2AM + 4BM^3 = \mu_o H \tag{14}$$

close to T_c in zero field, there is a net magnetization M_s, $M_s = -A/2B$, therefore:

$$M_s \approx \sqrt{a/2B}(Tc - T)^{1/2} \tag{15}$$

and given by equation (13) we can solve for the susceptibility M/H in the paramagnetic state:

$$\chi \approx (\mu_o/2a)(T - T_c)^{-1} \tag{16}$$

This explanation is called mean field theory for ferromagnetism, as they have validity for T near T_c. Weiss molecular field theory, also, obtains the same results. This relations are in general for any second order phase transition [2].

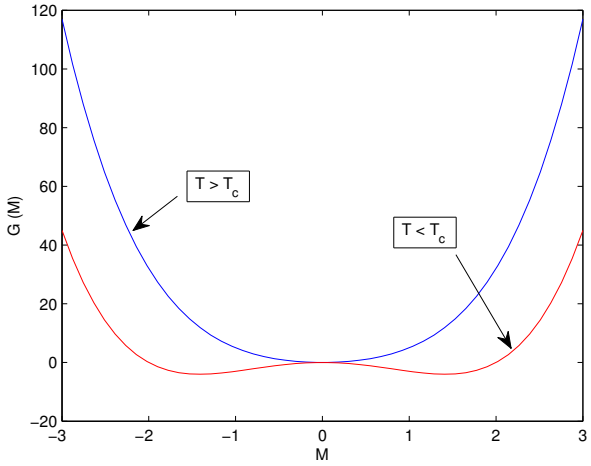

Figure 7: Free energy close to the critical temperature. For $T < T_c$ there is minimum value at $(\pm M_s)$, for $T > T_c$ minimum is at $M = 0$ paramagnetic state

2.3 Magnetic Interactions and magnetic energies

We present here the different magnetic interactions occurring in a crystal, which are responsible for the complexity of magnetic behavior.

2.3.1 Exchange Interaction

This interaction is due to quantum mechanics effect, or exclusion due to the symmetric parts of the two body wave function between two electrons. Mathematically can be expressed as:

$$J_{ab} = \langle \phi_a(\vec{r_i})\phi_b(\vec{r_j})|H_{ij}|\phi_b(\vec{r_i})\phi_a(\vec{r_j}) \tag{17}$$

where $\vec{r_i}$ and $\vec{r_j}$ are the position of the two electrons, ϕ_a and ϕ_b are the wave functions. H_{ij} is the repulsive Hamiltonian for the two atoms. Given that a system prefers minimum energy states, J_{ab} is positive for ferromagnetic, that means parallel disposition between spins is preferred. This interaction is the one responsible for ferromagnetic phenomena. The exchange interaction can be reformulated as Heisenberg proposed:

$$\hat{H} = 2J\hat{\mathbf{S}}_\mathbf{1} \cdot \hat{\mathbf{S}}_\mathbf{2} \tag{18}$$

Where J is the exchange integral of equation 20, which decays rapidly with distance, and can be treated as constant, and $\hat{\mathbf{S}}_\mathbf{1}$ and $\hat{\mathbf{S}}_\mathbf{2}$ are dimensionless spin operators [2, 7]. In a lattice, to obtain the total exchange energy we sum over all the electrons:

$$\hat{H} = 2\sum_{i \neq j} J_{ij}\hat{\mathbf{S}}_\mathbf{i} \cdot \hat{\mathbf{S}}_\mathbf{j} \tag{19}$$

At a mesoscopic level, assuming the length scale considered is much bigger that interatomic space. The exchange energy can be considered as follows:

$$\epsilon_{exc} = \frac{A}{V}\int (\nabla|\mathbf{m}|)^2 dV \tag{20}$$

where $\mathbf{m} = \mathbf{M}/M_s$ is the normalized magnetization, and A is the exchange stiffnes, which is related with the exchange constant and the lattice constant. Exchange interaction is minimum for $\mathbf{M}$ uniform[1]. The exchange field is given by:

$$\mathbf{H}_{ex} = \frac{2A}{M_s^2}\nabla^2\mathbf{M} \tag{21}$$

2.3.2 Zeeman Energy

Zeeman energy is the interaction of the magnetization, or each magnetic dipole, with an external magnetic field, $\mathbf{H}_{ext}$.

$$\epsilon_Z = \frac{\mu_o}{V}\int \mathbf{M} \cdot \mathbf{H}_{ext} \tag{22}$$

The energy is minimized when $\mathbf{M}$ and $\mathbf{H}_{ext}$ are aligned parallel [7].

2.3.3 Demagnetizing energy

This energy is due to the dipolar interaction between magnetic dipoles of the lattice, which is very long ranged compared to other interactions. This interaction gives rise the demagnetized field, which favor the closure of the magnetic flux inside the material. The energy of demagne-

tization can be written as follows:

$$\epsilon_{dem} = -\frac{\mu_o}{2V}\int_{sample} \mathbf{M}\cdot\mathbf{H}_{dem} \tag{23}$$

Where $\mathbf{H}_{dem}$ is the demagnetizing field, which is due to the shape of the sample. The calculation of $\mathbf{H}_{dem}$ can be cumbersome for a complex shape, but can be easily represented for some geometries which have uniform response, such as the case of an ellipsoid:

$$\mathbf{H}_{dem} = -N\mathbf{M} \tag{24}$$

where N is the demanatizing tensor, which can be diagonalized in the base which is parallel to the symmetry axis. In the general case for an ellipsoid we can write

$$N = \begin{pmatrix} N_x & 0 & 0 \\ 0 & N_y & 0 \\ 0 & 0 & N_z \end{pmatrix} \tag{25}$$

the trace of the demagnetizing tensor shloud be dimensionless and normalized, $N_x + N_y + N_z = 1$ [1].

2.3.4 Cubic Anisotropy Energy

In general the crystal lattice, arrange electrons such that there is a preferred direction for $\mathbf{M}$. This anisotropy energy is related with the direction of the magnetization respect to the crystal axes. This interaction can be written as follows:

$$\epsilon_{CA} = K_1(\cos^2\alpha\cos^2\beta + \cos^2\alpha\cos^2\gamma + \cos^2\beta\cos^2\gamma) + K_2(\cos^2\alpha\cos^2\beta\cos^2\gamma) \tag{26}$$

Where K_1, K_2 are anisotropy constants, and α, β, γ are the angles between the magnetization and the crystal axes. Depending on the signs of the constants, easy and hard axes of magnetization can be identified [7].

2.3.5 Uniaxial Anisotropy Energy

Similar to the cubic anisotropy energy, uniaxial anisotropy is related to magnetocrystalline anisotropies, when there is a known easy axis of magnetization.

$$\epsilon_u = K_u \sin^2\alpha \tag{27}$$

Where K_u is a constant, and α is the angle between magnetization vector and the easy axis [7]. The anisotropy field is written as follows:

$$\mathbf{H}_k = \nabla_{\mathbf{M}} \epsilon_u(\mathbf{M}) \tag{28}$$

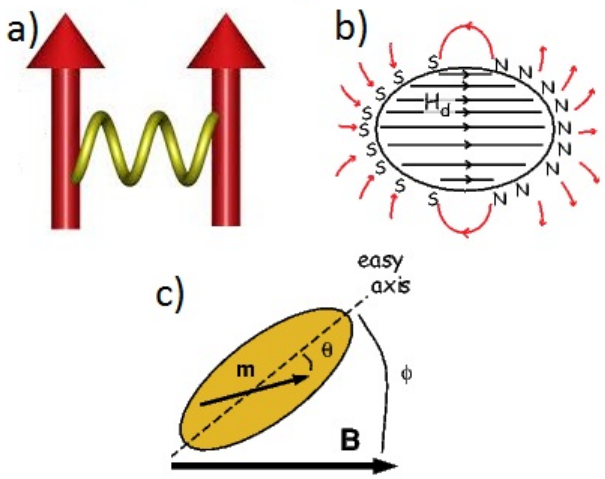

Figure 8: Skecth of magnetic interactions, a) Exchange interaction b) Demagnetizing field c) Anisotropy field

2.4 Effective Fiedl $\mathbf{H}_{eff}$

All the interactions previously introduced generates an effective field $\mathbf{H}_{eff}$, which is the field felt locally by an magnetic moment in matter. If we find what is the configuration, or magnetization, of the system that minimizes the energy, we will find the static state for $\mathbf{M}$. In this context, the effective field can be expressed as follow:

$$\mathbf{H}_{eff} = -\frac{1}{\mu_o} \nabla_{\mathbf{M}} \epsilon_{tot} = -\frac{1}{\mu_o} \left(\frac{\partial \epsilon_{tot}}{\partial M_x} \hat{M}_x + \frac{\partial \epsilon_{tot}}{\partial M_y} \hat{M}_y + \frac{\partial \epsilon_{tot}}{\partial M_z} \hat{M}_z \right) \tag{29}$$

where ϵ_{tot} is the sum of all the interaction energy terms. We can write the the effective field for all the interactions as follows:

$$\mathbf{H}_{eff} = \mathbf{H}_{ext} + \mathbf{H}_{dem} + \mathbf{H}_{ex} - \mathbf{H}_k \tag{30}$$

where $\mathbf{H}_{ext}$ is the external field, $\mathbf{H}_{dem}$ demagnetizing field, $\mathbf{H}_k$ the anisotropy field, and $\mathbf{H}_{ex}$ the exchange field.

3 Magnetization Dynamics: Uniform excitation

3.1 Landau - Lifshitz equation

Dynamics of magnetic domains can be expressed as the movement of a top produced by an external force. The angular momentum changes due to an "external force" or torque. In this context is the magnetization that changes due to a magnetic field ($\mathbf{H}_{eff}$), being $\mathbf{H}_{eff}$ the "force" and $\mathbf{M}$ "position". We can write the following equation:

$$\frac{d\mathbf{M}}{dt} = -\gamma\mu_o \mathbf{M} \times \mathbf{H}_{eff} \tag{31}$$

This equation says that the Magnetization vector precess around the effective field vector, see figure (9). This equation does not take into account any decaying process, which will be addressed later. An important feature of is that it states the conservation of the norm of $\mathbf{M}$, this can be shown if we take the inner product of equation (31), we obtain:

$$\frac{d\mathbf{M}^2}{dt} = 0 \tag{32}$$

This equation states that $\mathbf{M}$ moves in the surface of an sphere.

3.2 Linearization of Lifshitz-Landau equation

Now we will assume that the effective field and the magnetization are made of a static ($\mathbf{M}_o$, $\mathbf{H}_o$) and oscillating components ($\mathbf{m}$, $\mathbf{h}$).

$$\mathbf{M} = \mathbf{m} + \mathbf{M}_o \quad , \quad \mathbf{H} = \mathbf{h} + \mathbf{H}_o \tag{33}$$

with the property that $|M_o| \gg |m|$ and $|H_o| \gg |h|$. Replacing (33) in (31), and taking the approximation to zero order in $|m|$ and $|h|$. We obtain the zero approximation equation, which simply states in absence of oscillating fields the magnetization vector will take the parallel direction to the effective field [3].

$$\mathbf{M}_o \times \mathbf{H}_o = 0 \tag{34}$$

Using the method of successive approximations, lets take the first order approximation for equation (31). Leaving the terms of first order in $|m|$ and $|h|$, and using (34), we obtain:

$$\frac{d\mathbf{m}}{dt} + \gamma\mathbf{m} \times \mathbf{H}_o = \gamma\mathbf{h} \times \mathbf{M}_o \tag{35}$$

this is called the *linearized equation of motion*.

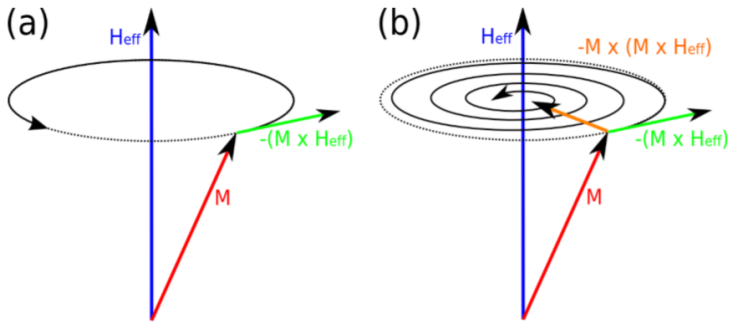

Figure 9: Sketch of a) the precession of $\mathbf{M}$ around $\mathbf{H}_{eff}$. b) Sketch shows the additional term that points toward $\mathbf{H}_{eff}$[1]

3.3 Gilbert Damping

Equation (31) does not take into account any dissipation process. We will adopt the common phenomenological approach. In figure (9), we see that a dissipation term should points toward the effective field vector, such that the amplitude decreases with time. This term is perpendicular to $\mathbf{M}$ and $-\mathbf{M} \times \mathbf{H}_{eff}$. To take into account dissipation we add a term, using normalized magnetization to preserve the norm of $\mathbf{M}$, to equation (31) [1, 3].

$$\frac{d\mathbf{M}}{dt} = -\gamma\mu_o \mathbf{M} \times \mathbf{H}_{eff} - \frac{\gamma\lambda}{M_s^2}\mathbf{M} \times (\mathbf{M} \times \mathbf{H}_{eff}) \tag{36}$$

Now replacing equation (31), in the second term of equation (36), we obtain the Landau-Lifshitz-Gilbert equation:

$$\frac{d\mathbf{M}}{dt} = -\gamma\mu_o \mathbf{M} \times \mathbf{H}_{eff} - \frac{\alpha}{M_s}\mathbf{M} \times \frac{d\mathbf{M}}{dt} \tag{37}$$

where α is the phenomenological Gilbert damping, which is a parameter to determine. This is a simplistic way to describe damping, which can be addressed from various relaxations processes such as spin-lattice scattering and spin-spin [6]. Constants of equation (37) are related with constants of equation (36) as follows:

$$\gamma \to \frac{\gamma}{1+\alpha^2} \qquad \lambda \to \frac{\alpha\mu_o M_s}{1+\alpha^2} \tag{38}$$

3.4 Dynamic Susceptibility Tensor for Thin film with out of plane External field

Solve LLG equation is not always easy for any geometry. We give the solution of LLG equation for a thin ferromagnetic film magnetized perpendicular to the plane with uniaxial anisotropy, as it is of interest for our project. The assumptions about the nature of the problem and also the geometry of the chosen sample are listed below:

- We will consider an infinite thin plane of ferromagnetic material, thin film, such that $N_x = N_y = 0$ and $N_z = 1$.
- Uniaxial Anisotropy, along the z-axis with constant K_p, which favor a little bit the out of plane direction for the magnetization.
- External static field is applied along z-axis.
- A weak microwave $\mathbf{h}$ field points along y-axis

This considerations allow us to say that $\mathbf{M}$ precess around $M_s\hat{z}$ (magnetization vector moves in the $x-y$ plane, while the z component keeps constant as it is saturated along this axis), such that $m_x \ll M_z$, $m_y \ll M_z$. Lets write the the normalized magnetization vector

$$\mathbf{M} = m_x\hat{x} + m_y\hat{y} + M_s\hat{z} \tag{39}$$

Now we can write the total magnetic energy for the system

$$\begin{aligned}\epsilon_{tot} &= -\mu_o\mathbf{M}\cdot(\mathbf{H}_{ext}+\mathbf{h}) + \frac{\mu_o}{2}M_z^2 - \frac{K_p}{d}\cos^2\alpha \\ &= -\mu_o\mathbf{M}\cdot(\mathbf{H}_{ext}+\mathbf{h}) + \frac{\mu_o}{2}(\mathbf{M}\cdot\hat{z})^2 - \frac{K_p}{M_s^2 d}(\mathbf{M}\cdot\hat{z})^2\end{aligned} \tag{40}$$

Now we use equation (29) to calculate $\mathbf{H}_{eff}$ resulting:

$$\begin{aligned}\mathbf{H}_{eff} &= \mathbf{H}_{ext} + \mathbf{h} - (\mathbf{M}\cdot\hat{z})\hat{z} + \frac{2K_p}{\mu_o M_s^2 d}(\mathbf{M}\cdot\hat{z})\hat{z} \\ &= h\hat{y} - \left(M_s - \frac{H_{ext}}{M_z} - \frac{2K_p}{\mu_o M_s d}\right)\frac{M_z}{M_s}\hat{z}\end{aligned} \tag{41}$$

We define the effective magnetization as $M_{eff} = M_s - H_k$ where H_k is the anisotropy field, and given that the sample is saturated along z-axis, $M_z = M_s$, we obtain the following equations, given by (31):

$$\begin{aligned}\frac{dm_x}{dt} &= -\gamma\mu_o m_y(H_{ext} - M_{eff}) + \gamma\mu_o M_s h - \alpha\frac{dm_y}{dt} \\ \frac{dm_y}{dt} &= -\gamma\mu_o m_x(H_{ext} - M_{eff}) + \alpha\frac{dm_x}{dt} \\ 0 &= -\gamma\mu_o m_x h + m_x\frac{dm_y}{dt} - m_y\frac{dm_x}{dt}\end{aligned} \tag{42}$$

As we did for the linearization of the equation in (35), we only take fist order approximation of the small quantities, as h, m_x, m_y. Now we will assume the equation goes to an steady state where all the terms oscillates with the same frequency as the h field. We will assume solutions of the form:

$$m_x = \widetilde{m_x}e^{i\omega t} \qquad m_y = \widetilde{m_y}e^{i\omega t} \qquad h = \widetilde{h}e^{i\omega t} \tag{43}$$

We obtain the following two equations, because third equation is not relevant in the first order approximation.

$$\begin{aligned} i\omega\widetilde{m_x} &= -\gamma\mu_o\widetilde{m_y}(H_{ext} - M_{eff}) + \gamma\mu_o M_s\widetilde{h} - \alpha i\omega\widetilde{m_y} \\ i\omega\widetilde{m_y} &= -\gamma\mu_o\widetilde{m_x}(H_{ext} - M_{eff}) + \alpha i\omega\widetilde{m_x} \end{aligned} \tag{44}$$

Introducing $\omega_H = \gamma\mu_o(H_{ext} - M_{eff})$ and $\omega_M = \gamma\mu_o M_s$. We can write the system as a matrix:

$$\begin{pmatrix} \omega_H + i\alpha\omega & -i\omega \\ i\omega & \omega_H + i\alpha\omega \end{pmatrix} \begin{pmatrix} \widetilde{m_x} \\ \widetilde{m_y} \end{pmatrix} = \omega_M \begin{pmatrix} 0 \\ \widetilde{h} \end{pmatrix} \tag{45}$$

We can solve this system for $\mathbf{M}$ simply inverting the matrix, which gives the Polder susceptibility tensor ($\overleftrightarrow{\chi}$), that information of the amplitude and phase of the oscillation of $\mathbf{M}$ in response to an escitation $\mathbf{h}$.

$$\overleftrightarrow{\chi} = \frac{\omega_M}{\omega_H^2 - \omega^2 + 2\alpha\omega_H\omega i} \begin{pmatrix} \omega_H + i\alpha\omega & -i\omega \\ i\omega & \omega_H + i\alpha\omega \end{pmatrix} \tag{46}$$

We assume α to be smaller such that $1 \approx 1+\alpha^2$. from equation (46), we see that as we expect the oscillating field h is parallel to the y component of M. Lets analyze the term χ_{yy} of the tensor that will give us the amplitude of the oscillation. Lets break it in two terms $\chi_{yy} = \chi'_{yy} - i\chi''_{yy}$, a real and a imaginary part.

$$\begin{aligned} \chi'_{yy} &= -\frac{\omega_M\omega_H(\omega_H^2 - \omega^2)}{(\omega_H^2 - \omega^2)^2 + (2\alpha\omega_H\omega)^2} \\ \chi''_{yy} &= -\frac{\alpha\omega\omega_M(\omega_H^2 + \omega^2)}{(\omega_H^2 - \omega^2)^2 + (2\alpha\omega_H\omega)^2} \end{aligned} \tag{47}$$

We can see that for $\omega = \omega_H$ the real part vanish, and the imaginary part has its maximum value, this is called the *resonance frequency*, which is given by $\omega_{res} = \gamma\mu_o(H_{ext} - M_{eff})$ for this special case of a thin film with perpendicular to the plane external field. Also, we can see that the real part of h is in phase with the magnetization y-component, but the imaginary part are $\pi/2$ out of phase. Replacing $\omega = \omega_H$ in (47), we obtain the maximum value of χ''_{yy}

$$Max(\chi''_{yy}) = \frac{\omega_M}{2\alpha\omega_H} \tag{48}$$

Also we can relate the width of χ''_{yy} at half height, which is related directly with the damping coefficient as follows.

$$\Delta\omega \approx 2\alpha\omega_{res} \tag{49}$$

which stands for any geometry. The resonance frequency obtained here is special case of a well

known formula, called Kittel formula[1], which is derived assuming a geometry of an ellipsoid:

$$\omega_{res}^2 = (\omega_H + (N_x - N_z)\omega_M)(\omega_H + (N_y - N_z)\omega_M) \tag{50}$$

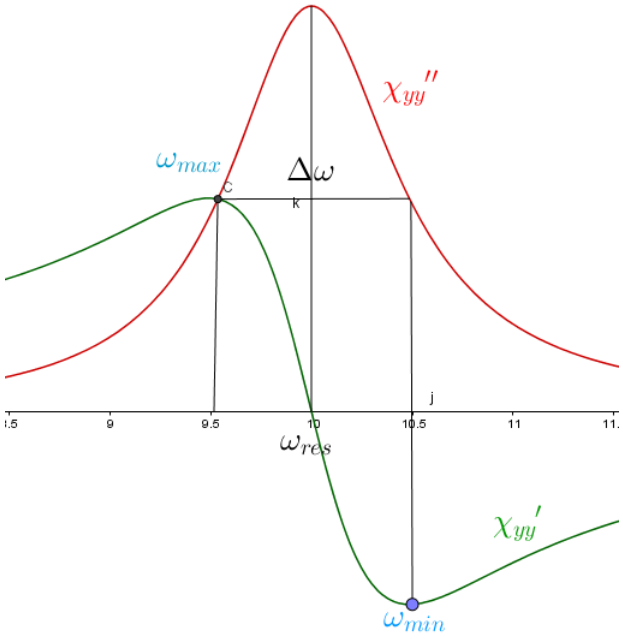

Figure 10: Real and imaginary part of the term χ_{yy} of the susceptibility tensor. Imaginary part has a Lorentzian lineshape, and is the responsible of the damping of the precession. Real part is the derivative of a Lorentzian.

4 Spin Waves: Non-Uniform excitation

4.1 Electromagnetic waves in Anisotropic Media

Electromagnetism is governed by Maxwell's equations, we can write them for anisotropic linear materials as follows:

$$\begin{aligned} \nabla \times \mathbf{H} = \frac{\partial \mathbf{D}}{\partial t} + \mathbf{J} \qquad & \nabla \times \mathbf{E} = -\frac{\partial \mathbf{B}}{\partial t} \\ \nabla \cdot \mathbf{D} = \rho \qquad & \nabla \cdot \mathbf{B} = 0 \end{aligned} \tag{51}$$

where $\mathbf{J}$ is the free current density, ρ is he free charge density, and:

$$\begin{aligned} \mathbf{D} &= \epsilon_o \mathbf{E} + \mathbf{P} \\ \mathbf{B} &= \mu_o(\mathbf{H} + \mathbf{M}) \end{aligned} \tag{52}$$

$\mathbf{P}$ is the density of electric dipoles, or polarization, and $\mathbf{M}$ is the magnetization. For linear medium there is a linear relation between the polarization and electric field, and the magnetization and external field.

$$\begin{aligned} \mathbf{P}(\omega) &= \epsilon_o \overleftrightarrow{\chi_\mathbf{e}}(\omega) \cdot \mathbf{E}(\omega) \\ \mathbf{M}(\omega) &= \overleftrightarrow{\chi_\mathbf{m}}(\omega) \cdot \mathbf{H}(\omega) \end{aligned} \tag{53}$$

where for steady state solutions, as we state before, depends only on the the frequency of oscillation ω, for field that varies as $\propto \exp(i\omega t)$. Here we identify $\overleftrightarrow{\chi_\mathbf{e}}$ as the electric susceptibility, and $\overleftrightarrow{\chi_\mathbf{m}}$ as the magnetic susceptibility. We can define the following relations:

$$\begin{aligned} \mathbf{D} &= \overleftrightarrow{\epsilon} \cdot \mathbf{E} \\ \mathbf{B} &= \overleftrightarrow{\mu} \cdot \mathbf{H} \end{aligned} \tag{54}$$

where

$$\begin{aligned} \overleftrightarrow{\epsilon} &= \epsilon_o(\overleftrightarrow{I} + \overleftrightarrow{\chi_e}) \\ \overleftrightarrow{\mu} &= \mu_o(\overleftrightarrow{I} + \overleftrightarrow{\chi_m}) \end{aligned} \tag{55}$$

where $\overleftrightarrow{I}$ is the identity tensor. These are called respectively, the permittivity and permeability tensors, which are hermitian tensors in order to satisfy Complex Poynting's theorem[4]. So far we have consider static oscillations and uniform excitations, now we will consider waves in magnetic media, as ferrites. For that we take plane wave solutions of the form $\exp[i(\mathbf{k}\cdot\mathbf{r} - \omega t)]$, where $\mathbf{k}$ is the wave vector that represents the direction of propagation of the wave. Making the EM fields being plane waves, Maxwell's equations transforms as follows:

$$\begin{aligned} i\mathbf{k} \times \mathbf{H} = -i\omega\mathbf{D} + \mathbf{J} \qquad & \mathbf{k} \times \mathbf{E} = \omega\mathbf{B} \\ i\mathbf{k} \cdot \mathbf{D} = \rho \qquad & \mathbf{k} \cdot \mathbf{B} = 0 \end{aligned} \tag{56}$$

Lets consider source-free nonconductive media, such that, $\rho = 0$ and $\mathbf{J} = 0$, and using relations (55), we obtain:

$$\begin{aligned} \mathbf{k} \times \mathbf{H} &= -\omega \overleftrightarrow{\epsilon} \cdot \mathbf{E} \\ \mathbf{k} \cdot \mathbf{E} &= \omega \overleftrightarrow{\mu} \cdot \mathbf{H} \end{aligned} \tag{57}$$

4.2 Magnetostatic Approximation

Lets consider a field composed of a small oscillating field $\mathbf{h}$ and a strong static field $\mathbf{H}$, so we can write equations (56) in the case of an isotrope linear magnetic material, as:

$$\begin{aligned} \mathbf{k} \times \mathbf{h} &= -\omega \epsilon \mathbf{e} \\ \mathbf{k} \cdot \mathbf{e} &= \omega \mu_o (\mathbf{h} + \mathbf{m}) \end{aligned} \tag{58}$$

taking the cross product of equation (1.58) with $\mathbf{k}$, we obtain:

$$\mathbf{k}(\mathbf{k} \cdot \mathbf{h}) - \mathbf{k}^2 \mathbf{h} = -\omega^2 \epsilon \mu_o (\mathbf{h} + \mathbf{m}) \tag{59}$$

Since $\mathbf{k} \cdot \mathbf{b} = 0$, we have $\mathbf{k} \cdot h = -\mathbf{k} \cdot \mathbf{m}$ replacing this and solving for $\mathbf{h}$ we have, and replacing $k_o = \sqrt{\omega^2 \epsilon \mu_o}$. $\mathbf{k}$ is the wave vector of the magnetic excitation, e.g. spin wave, while k_o is the wave vector of the EM wave that produces the excitation, e.g. microwave signal:

$$\mathbf{h} = \frac{k_o^2 \mathbf{m} - \mathbf{k}(\mathbf{k} \cdot \mathbf{m})}{k^2 - k_o^2} \tag{60}$$

doing the same for equation (2.58), and solving for $\mathbf{e}$, we obtain:

$$\mathbf{e} = -\frac{\omega \mu_o \mathbf{k} \times \mathbf{m}}{k_o^2 - k^2} \tag{61}$$

and using the relation between $\mathbf{h}$ and $\mathbf{e}$, we obtain:

$$\nabla \times \mathbf{h} = -\frac{k_o^2 \mathbf{k} \times \mathbf{m}}{k_o^2 - k^2} \tag{62}$$

In general for frequencies that produces ferromagnetic occurs in the microwave frequency range for which the electromagnetic wave vector is of the order $k_o \sim cm^{-1}$. While, spin wave vector is tipically of the order $k \sim \mu m^{-1}$ in our project, then we have $k \gg k_o$. We can approximate the rotational of $\mathbf{h}$ as:

$$\nabla \times \mathbf{h} = 0 \tag{63}$$

which is called the magnetostaic approximation, from which we can define a scalar potential $\psi(\mathbf{r}, t)$ such that $\mathbf{h} = -\nabla \psi$.

4.3 Walker's Equation

The equations of magnetoquaistatics derived in the last section are:

$$\nabla \times \mathbf{h} = 0 \tag{64}$$

$$\nabla \cdot \mathbf{b} = 0 \tag{65}$$

$$\nabla \times \mathbf{e} = i\omega \mathbf{b} \tag{66}$$

Now we have to determine the dispersion relation of the media, which we consider to be a ferromagnetic material,

$$\mathbf{b} = \overleftrightarrow{\mu} \cdot \mathbf{h} \tag{67}$$

where

$$\overleftrightarrow{\mu} = \mu_o(\overleftrightarrow{I} + \overleftrightarrow{\chi}) \tag{68}$$

where χ is the susceptibility tensor as defined in section 1.5.3, with $\alpha = 0$. Now, given that $\mathbf{h}$ is irrotational we can define a magnetostatic scalar potential such that $\mathbf{h} = -\nabla\psi$, we obtain Walker's equation:

$$\nabla \cdot (\overleftrightarrow{\mu} \cdot \nabla\psi) = 0 \tag{69}$$

if we consider the susceptibility tensor without damping, and neglecting exchange interaction as:

$$\overleftrightarrow{\mu} = \mu_o \begin{pmatrix} 1+\chi & -i\kappa & 0 \\ i\kappa & 1+\chi & 0 \\ 0 & 0 & 1 \end{pmatrix} \tag{70}$$

where

$$\chi = \frac{\omega_M \omega_H}{\omega_H^2 - \omega^2} \tag{71}$$

$$\kappa = \frac{\omega_M \omega}{\omega_H^2 - \omega^2} \tag{72}$$

This can be expanded to:

$$(1+\chi)\left[\frac{\partial^2\psi}{\partial x} + \frac{\partial^2\psi}{\partial y}\right] + \frac{\partial^2\psi}{\partial z} = 0 \tag{73}$$

for which the plane wave solution $\psi \propto \exp(i\mathbf{k} \cdot \mathbf{r})$ gives:

$$(1+\chi)(k_x^2 + k_y^2) + k_z^2 = 0 \tag{74}$$

This equation gives a frequency band for which the magnetostatic volume waves solution exists[6]:

$$\omega_H \leq \omega \leq \sqrt{\omega_H^2 + \omega_H \omega_M} \tag{75}$$

4.4 Normally magnetized film

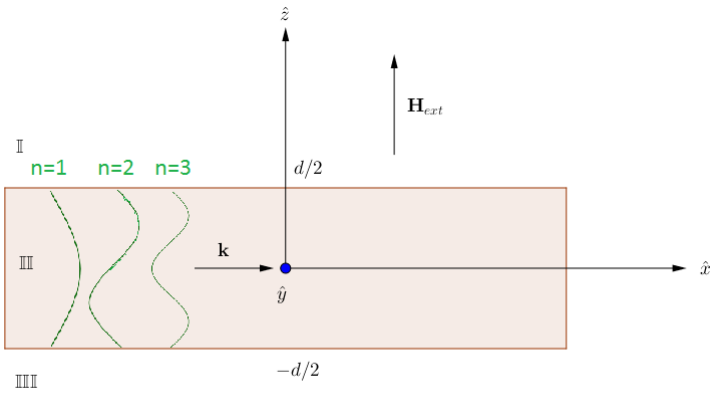

Figure 11: Thin film of ferromagnetic material magnetized along z-axis. A wave in the film can be analyzed as planes waves bouncing between the surfaces of the film, which can be seen as standing waves along the thickness.

Lets suppose we have a film of ferromagnetic material of thickness d, which is magnetized along the z-axis. The wave vector is decomposed in transversal wave vector $\mathbf{k}_t$ and the perpendicular wave vector $k_z\hat{z}$, where $\mathbf{k} = \mathbf{k}_t + k_z\hat{z}$, and for the reflected wave $\mathbf{k} = \mathbf{k}_t - k_z\hat{z}$. If we wait long enough, system will go to steady state, which can be seen as plane waves bouncing back and forth between the boundaries of the film. We can set as a trial solution for region 𝕀𝕀𝕀 of the scalar function, a superposition of bouncing plane waves:

$$\psi_{II}(\mathbf{r}) = \psi_o e^{i\mathbf{k}\cdot\mathbf{r}}\left[\frac{e^{ik_z z} + e^{-ik_z z}}{2}\right] = \psi_o e^{i\mathbf{k}\cdot\mathbf{r}}\cos(k_z z) \tag{76}$$

For regions 𝕀 and 𝕀𝕍, $\chi = 0$, Walker's equation reduces to Laplace's equation ($\nabla^2\psi = 0$). This leads to $k_{z,d} = \pm ik_{t,d}$, where the subscript d refers to the dielectric regions ($\chi = 0$). For regions 𝕀 and 𝕀𝕍 waves should vanish as $z = \pm\infty$, we can write the following trial solutions:

$$\psi_I = Ce^{i\mathbf{k}_{t,d}\cdot\mathbf{r} - k_{t,d}z} \tag{77}$$

$$\psi_{III} = De^{i\mathbf{k}_{t,d}\cdot\mathbf{r} + k_{t,d}z} \tag{78}$$

Now we must use boundary conditions of electromagnetism. This boundary conditions are easily derived from Maxwell's equations. These conditions are:

- tangential component of $\mathbf{h}$ is continuous.
- normal component of $\mathbf{b}$ is continuous.

First condition follows from the fact that there is no surface currents in the film, which is an electric insulator. Tangential component of $\mathbf{h}$ comes from $\mathbf{h}_t = \nabla_t\psi$. Requiring $\mathbf{h}_t$ to be

continuous at $z = \pm d/2$:

$$-i\mathbf{k}_{t,d}\psi_I(z = d/2) = -i\mathbf{k}_t\psi_{II}(z = d/2) \tag{79}$$

$$-i\mathbf{k}_{t,d}\psi_{III}(z = -d/2) = -i\mathbf{k}_t\psi_{II}(z = -d/2) \tag{80}$$

These equalities are valid for all x, y only for $\mathbf{k}_{t,d} = \mathbf{k}_t$, Equations (79) y (80) transform into:

$$Ce^{-k_t d/2} = \psi_o cos(k_z d/2) \tag{81}$$

$$De^{-k_t d/2} = \psi_o cos(k_z d/2) \tag{82}$$

from which we can conclude that $C = D$. Now making that normal component of $\mathbf{b}$ must be continuous, we have:

$$k_t Ce^{-k_t d/2} = \psi_o k_z sin(k_z d/2) \tag{83}$$

$$-k_t De^{-k_t d/2} = -\psi_o sin(k_z d/2) \tag{84}$$

with $C = D$, this two equations are not independent, so we only have two independent equations, which can be combined to obtain:

$$\tan(k_z d/2) = \frac{k_t}{k_z} \tag{85}$$

k_t and k_z are related by (74), so we obtain the following implicit dispersion relation

$$\tan\left[\frac{k_t d}{2}\sqrt{-(1+\chi)}\right] = \frac{1}{\sqrt{-(1+\chi)}} \tag{86}$$

which can be solved graphically, considering the crossing of the functions at both sides of the equation. This means that there exist multiple modes of the waves, as the tangent has a periodicity, this solutions are for even scalar functions, taking into account odd modes we can write a single dispersion relation, for any mode:

$$\tan\left[\frac{k_t d}{2}\sqrt{-(1+\chi)} - \frac{n\pi}{2}\right] = \frac{1}{\sqrt{-(1+\chi)}} \tag{87}$$

Kalinikos [5] obtained a useful approximation of the dispersion relation, for the lowest mode $n = 0$:

$$\omega^2 = \omega_H\left[\omega_H + \omega_M\left(1 - \frac{1 - e^{-k_t d}}{k_t d}\right)\right] \tag{88}$$

for this mode, the group velocity which represents the velocity of the spin wave is:

$$v_g = \frac{\omega_H\omega_M}{2\omega k_t d}\left[\frac{1}{k_t} - \left(\frac{1}{k_t} + d\right)e^{-k_t d}\right] \tag{89}$$

Now we can summarize the results for this mode:

- This wave modes have all the same cutoff frequency, which means there is no range of frequencies where only a single mode propagates, for low enough k vectors such that we can neglect exchange interaction. This range is given by equation (75).
- The group and phase velocity have both the same direction, this is the characteristic of *Forward waves*.
- the wave amplitude is distributed through all the volume of the film.

Therefore this mode is called *magnetostatic forward volume waves*(MFVW's)[5].

4.5 Tangentially magnetized film: Backward Volume Waves

When external field is applied in plane, and parallel to the $\mathbf{k}$ vector as figure (12) shows, doing the same considerations as the last section we obtain the following implicit dispersion relation:

$$\tan\left[\frac{k_z d}{2\sqrt{-(1+\chi)}} - \frac{(n-1)\pi}{2}\right] = \sqrt{-(1+\chi)} \tag{90}$$

Kalinikos[5] obtained an approximation to equation (90), that can be solved explicitly for ω:

$$\omega^2 = \omega_H \left[\omega_H + \omega_M \left(\frac{1-e^{-k_t d}}{k_t d}\right)\right] \tag{91}$$

and the group velocity is:

$$v_g = -\frac{\omega_H \omega_M}{2\omega k_t d}\left[\frac{1}{k_t} - \left(\frac{1}{k_t} + d\right) e^{-k_t d}\right] \tag{92}$$

Summarizing this mode has the following characteristics:

- This wave modes have all the same cutoff frequency, which means there is no range of frequencies where only a single mode propagates. This range is given by equation (75).
- The group and phase velocity points in opposite directions, this is the characteristic of *backward waves*.
- the wave amplitude is distributed through all the volume of the film.

Therefore this mode is called *magnetostatic backward volume waves*(MBVW's)[5].

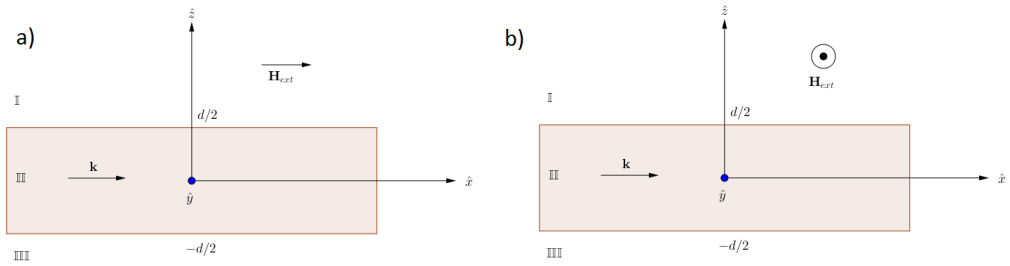

Figure 12: Thin film of ferromagnetic material magnetized along x-axis. Wave modes depend od the relative direction of the $\mathbf{k}$ vector. a) $\mathbf{H}_{ext} \parallel \mathbf{k}$ the mode is Backward volume waves. b) $\mathbf{H}_{ext} \perp \mathbf{k}$ the mode is Surface waves

4.6 Tangentially magnetized film: Surface Waves

When external field is applied in plane, and perpendicular to the $\mathbf{k}$ vector as figure(12) shows, doing the same considerations as the last section we obtain the following dispersion relation:

$$e^{-2kd} = \frac{(\chi+2)^2 - \kappa^2}{\chi^2 - \kappa^2} \tag{93}$$

Solving explicitly for ω^2:

$$\omega^2 = \omega_H(\omega_H + \omega_M) + \frac{\omega_M^2}{4}\left[1 - e^{-2kd}\right] \tag{94}$$

and the group velocity is:

$$v_g = \frac{\omega_M^2 d}{4\omega} e^{-2k_t d} \tag{95}$$

This mode has the property that when the direction of the $\mathbf{k}$ is switched, the mode energy is shifted to the opposite surface. This phenomenon is called *field displacement non-reciprocity*, and also the amplitude of the wave vanishes at the interior of the film. Summarizing this mode has the following characteristics:

- There is only a single propagating mode for a given frequency, in opposition to forward and backward volume modes. The range of frequencies is above than for volume modes, $\sqrt{\omega_H(\omega_H + \omega_M)} \leq \omega(k) \leq \omega(k = \infty)$ [6].
- The group and phase velocity points in the same direction. It is a forward wave.
- the wave amplitude decays exponentially from the surface of the film.

Therefore this mode is called *magnetostatic Surface Waves*(MSW's)[5].

5 Experimental Techniques

In this section we will present the experimental techniques we used to characterize ferromagnetic materials. Ferromagnetic resonance in thin films using diode detection with lock-in amplification, and a Vector Network Analyzer(VNA) . We also introduce technique to excite and detect spin waves via the Propagating Spin Wave Spectroscopy(PSWS).

5.1 Ferromagnetic Resonance

Ferromagnetic Resonance (FMR) is a technique vastly used and studied to characterize the magnetic properties of ferromagnetic materials. In general the technique consists in the use of an external static magnetic field, produce by an electromagnet, and an small oscillating field, created by a waveguide that supports transmission of high frequency microwave current. When frequency of the oscillating field matches with the resonance condition the reflected wave has an increase in power. In this thesis we use a VNA for FMR characterization and spin wave propagation. We also developed a FMR set up that uses diode detection with lock-in amplification. We will now present in more detail these techniques.

Coplanar Wave Guide

Ferromagnetic resonance on thin films is widely done with coplanar wave guides (CPW). As the name shows this wave guides are coplanar and in general is divided in one central line, and two ground lines at each side of the central one, see figure (13). CPW support Transverse Electric Magnetic modes for the range of frequencies used in ferromagnetic resonance, for higher frequencies is no longer the case.

It is possible to show that the inductance and capacitance of a CPW is [1]:

$$L = \frac{\mu_o}{4} f(s,w) \qquad C = 4\bar{\varepsilon}\frac{1}{f(s,w)} \tag{96}$$

where $f(s,w)$ is a conformal function of the dimensions of the CPW, and $\bar{\varepsilon}$ is the effective permittivity of the substrate. We define the phase velocity and the characteristic impedance of the line as follow (for more details see Appendix A):

$$v_{ph} = \frac{1}{\sqrt{\mu_o \bar{\varepsilon}}} \qquad Z_c = \frac{1}{4}\sqrt{\frac{\mu_o}{\bar{\varepsilon}}} f(s,w) \tag{97}$$

The important dimensions in a CPW, are the width of the signal line w, and the distance between signal and ground lines s. Ground lines have both width $w/2$, so that the net current density is zero through a cross section of the CPW. For millimteric size of S and G lines, the excitation will be almost uniform, while for micrometric size CPW will create non-uniform excitation

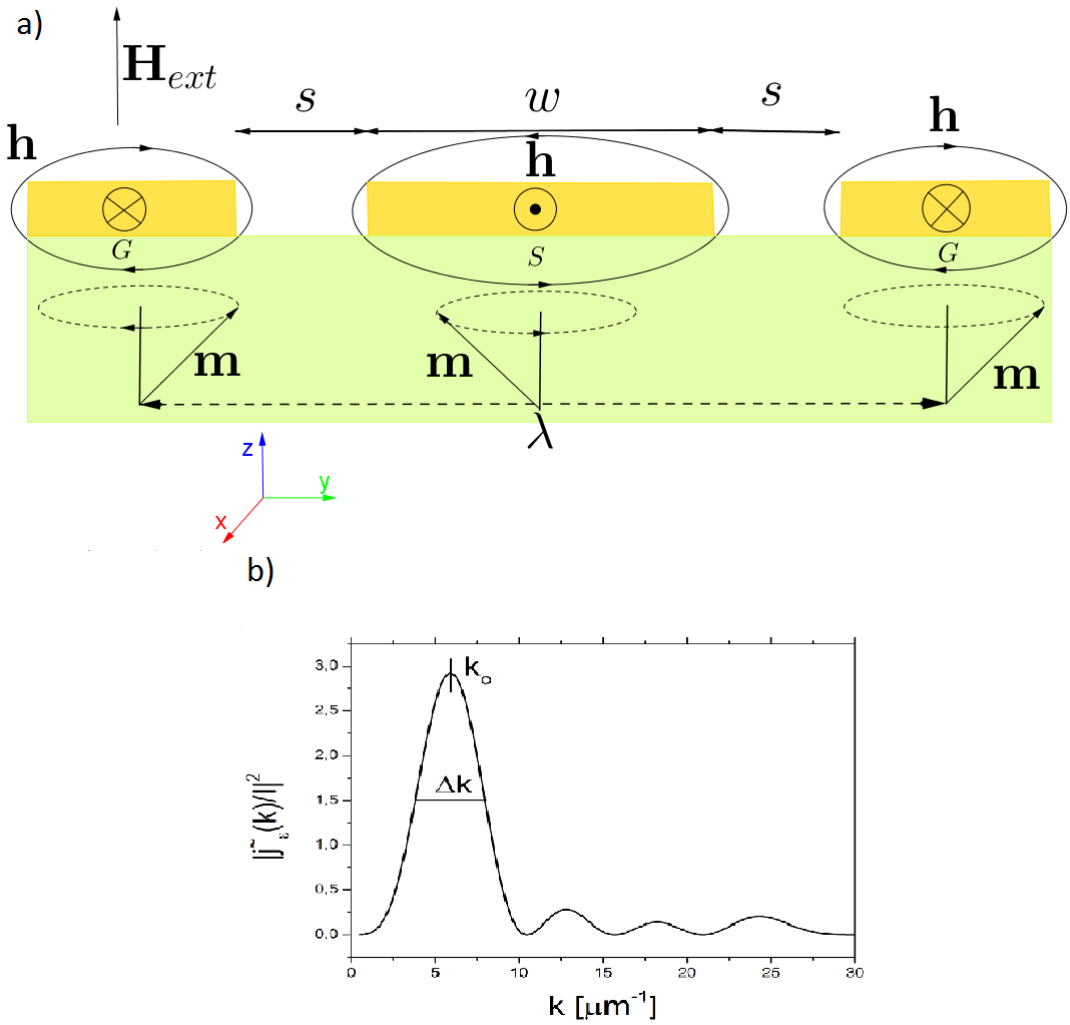

Figure 13: a) Coplanar Waveguide, the current trough creates the small oscillating field necessary to induce Resonance. b) Normalized Fourier transform of the current density in a single CPW line with $w = 400nm$ and $s = 200nm$

with k vector as the Fourier transform in figure (13) shows. The fabrication process should aim to obtain a characteristic impedance $Z_c = 50\,\Omega$ of the CPW to avoid reflection of signal, and therefore lose of it. Some CPW are built over an spacer of insulating material, because most of ferromagnetic material is a conductor an having the CPW in contact with the ferromagnetic material will short the circuit. In our case, we use YIG thin films with thickness $t = 29\,nm$, that were grown at Argonne National Laboratory. On Gadolinium Gallium Garnet (GGG) substrate bears the YIG film. In this case, it is not necessary to use an spacer because YIG is an insulating material.

5.1.1 Lock in Amplification with Amplitude Modulation

This work started with the setup of a FMR station for the characterization of ferromagnetic thin films. This experiment was built in the solid state physics laboratory at the USFQ. The setup is

equipped with a $175\,W$ Power supply ($25\,V$, $7\,A$), a large resistive electromagnet (gap size $5\,cm$, pole diameter $20\ cm$), a DTM-151 Teslameter Group 3 with a Hall probe, a Wiltron 10MHz - 40GHz microwave sweep generator, 7265 DSP lock-in amplifier and Anritsu RF detector Model 75AV50 10MHz - 50GHz, see figure (14). Apparatus are controlled by programme interface via GPIB connection.

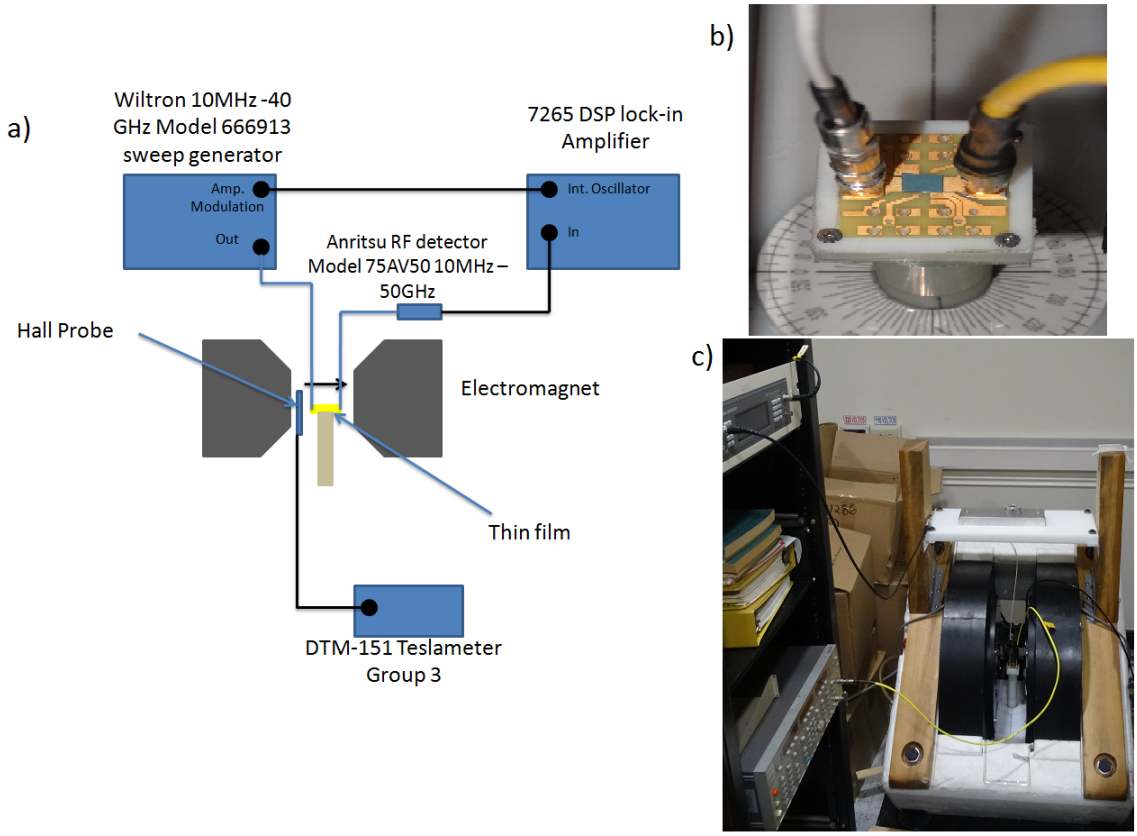

Figure 14: a) Set up of the FMR station using diode detection, lock-in amplification and amplitude modulation of the microwave signal. b) Picture of the CPW with a thin film of permalloy. c) Picture, showing the electromagnet and the rack for the generator and lock-in amplifier, of FMR set up in the Laboratory of Solid State Physics at USFQ.

We use SMA cables to propagate microwave signal through the CPW which is detected by the microwave diode. The ferromagnetic thin film is place face down on the CPW. Microwave input power is kept low ($-12\,dBm$) in order to stay in linear regime. The voltage drop due to the power absorption at resonance is of the order of μV. To obtain a better signal to noise ratio, we use modulation of the microwave signal with the low frequency internal oscillator of the lock-in amplifier. The lock-in amplifier detection is a technique useful to measure low amplitude signals. The lock in detector use a reference signal V_{ref}, created by an internal oscillator.

$$V_{ref} = V_{ref}\sin(\omega_r t + \theta_{ref}) \tag{98}$$

and the diode signal V_{sig} has a phase θ_{sig}

$$V_{sig} = V_{sig}\sin(\omega_s t + \theta_{sig}) \tag{99}$$

The phase of the reference signal ,θ_{ref}, is known. These two signals are mixed, we obtain:

$$\begin{aligned} V_{psd} &= V_{ref}V_{sig}\sin(\omega_r t + \theta_{ref})\sin(\omega_s t + \theta_{sig}) \\ &= \frac{1}{2}V_{sig}V_{ref}[\cos((\omega_r - \omega_s)t + \theta_{ref} - \theta_{sig})\cos((\omega_r + \omega_s)t + \theta_{ref} + \theta_{sig})] \end{aligned} \tag{100}$$

V_{psd} passes trough a low pass filter, this will remove the AC component. If the frequency of the reference and the diode signal is equal, we obtain:

$$V_{psd} = \frac{1}{2}V_{ref}V_{sig} \tag{101}$$

We programmed a labview interface that performs series of field sweeps spectrum for various frequencies In figure (15), we show two typical spectra at frequency of $3.25\,GHz$ and of

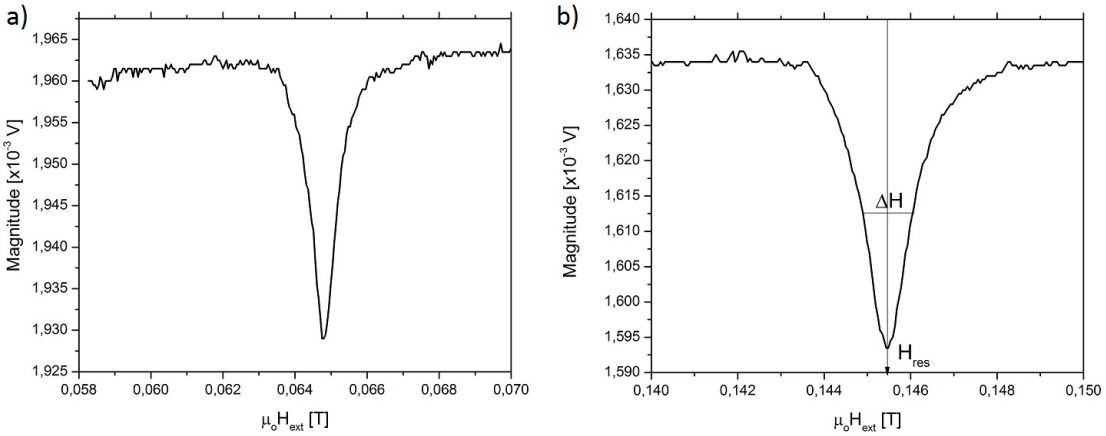

Figure 15: Spectra of power absorption of microwave signal due to ferromagnetic resonance of YIG thin films. a) $f_{res} = 3.25\,GHz$ b) $f_{res} = 5.75\,GHz$

$5.75\,GHz$, which show a decrease of the diode voltage of the order of $30\,\mu V$ due to power absorbed at resonance. With the power supply we have, we are able to measure FMR of YIG up to $7\,GHz$. We summarize the peak position and linewidth of the FMR peaks in figure (16). The magnitude of the power absorbed is related to the external $\mathbf{h}$ field, which has a linear relation with amplitude of the precession through the susceptibility tensor diagonal term (χ). For this setup, the field is applied in the plane of the film, the resonance condition assuming there is not in plane magnetocrystalline anisotropy, is given by Kittel formula (50):

$$\omega_{res} = \gamma\mu_o\sqrt{H_{ext}(H_{ext} + M_{eff})} \tag{102}$$

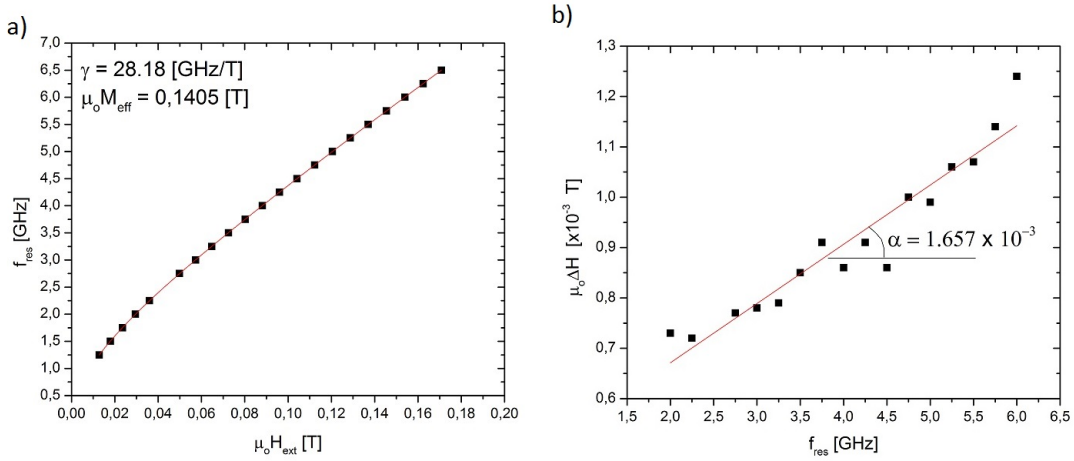

Figure 16: Spectra of power absorption of microwave signal due to ferromagnetic resonance. a) Fitting of Kittel's formula for in plane field in thin films FMR. b) Determination of the damping coefficient(α) from the linewidth of the resonance curve.

where ω_{res} is the resonance frequency, H_{ext} is the applied external field and $M_{eff} = M_s - H_k$ is the effective saturation magnetization of the film and H_k is the anisotropy field. We use equation (102) to fit the $f_{res}(H_{ext})$ data, from which we found an effective magnetization $\mu_o M_{eff} = \mu_o(M_s - H_k) = 0.14\,T$, and a gyromagnetic ratio $\gamma = 28.18\,GHz/T$. Using a linear regression to fit the linewidth $\Delta H(f_{red})$ gives us, which according to equation (52), the Gilbert damping coefficient $\alpha = 1.67 \times 10^{-3}$. We also observed a non-negligible inhomogeneous broadening (the interception of the line with the frequency axis) of $\mu_o \Delta H_o = 4.36 \times 10^3\,T$. This additional broadening is due to the magnetic inhomogeneities in the film.

5.1.2 Ferromagnetic Resonance in thin films via Vector Network Analyzer detection

5.1.3 Vector Network Analyzer

Vector Network Analyzer is an apparatus that generates and also detects microwave signal using detection lock in phase with an internal oscillator. When the transmitted wave is not a TEM mode, then it is not possible to define a voltage or current in the lines. In this case we work with the scattering matrix, which relates the transmitted and received signal of 2 ports. The device under test (DUT) is connected tot he 2 ports of the VNA.

The complex normalized amplitudes at each port are:

$$a_i = \frac{V_i + Z_{ci} I_i}{2\sqrt{Z_{ci}}} \qquad b_i = \frac{V_i - Z_{ci} I_i}{2\sqrt{Z_{ci}}} \tag{103}$$

Solving for V_i and I_i, we obtain:

$$V_i = \sqrt{Z_{ci}}(a_i + b_i) \tag{104}$$

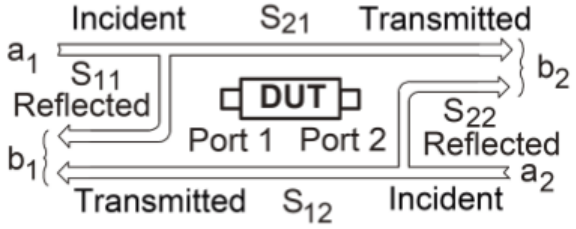

Figure 17: Schemme of a DUT showing the ongoing and outgoing waves in each port, credits: [1].

$$I_i = \frac{a_i - b_i}{\sqrt{Z_{ci}}} \tag{105}$$

Introducing equations (132) and (133) for V_i and I_i, see appendix A:

$$a_i = \frac{V_i^+}{Z_{ci}} e^{-\gamma x} \qquad b_i = \frac{V_i^-}{Z_{ci}} e^{\gamma x} \tag{106}$$

Which clearly show that a_i and b_i are out-going and out-coming waves. Now these waves for a 2 port DUT are related as follows:

$$\begin{pmatrix} b_1 \\ a_1 \end{pmatrix} = \bar{S} \begin{pmatrix} a_1 \\ a_2 \end{pmatrix} = \begin{pmatrix} S_{11} & S_{12} \\ S_{21} & S_{22} \end{pmatrix} \begin{pmatrix} a_1 \\ a_2 \end{pmatrix} \tag{107}$$

This relation satisfies that the off diagonal terms of the S-matrix are the same unless there is a specific nonreciprocal phenomena such as the one exhibited by magnetostatic surface waves. The microwave signal is in phase locked with an internal oscillator. When the microwaves pass trough the DUT, some of it is reflected, which then goes through a coupler. this signal is mixed with the internal oscillator signal to extract the phase and the amplitude of the reflected signal (S_{11}). Similarly, the transmitted signal is also mixed with internal oscillator signal to extract the phase and the amplitude(S_{21}). Finally, the variation of the S parameters allow to extract the change in impedance and inductance. The relation between the S-parameters and the Impedance Z matriz components Z_{ij} is given by[1, 6]:

$$Z_{ii} = Z_c \frac{(1 + S_{ii})(1 - S_{jj} + S_{ij}S_{ji})}{(1 - S_{ii})(1 - S_{jj}) - S_{ij}S_{ji}} \tag{108}$$

.

$$Z_{ij} = Z_c \frac{2S_{ij}}{(1 - S_{ii})(1 - S_{jj}) - S_{ij}S_{ji}} \tag{109}$$

. This elements define the matrix of Impedance which relates:

$$\begin{pmatrix} V_1 \\ V_1 \end{pmatrix} = \begin{pmatrix} Z_{11} & Z_{12} \\ Z_{21} & Z_{22} \end{pmatrix} \begin{pmatrix} I_1 \\ I_2 \end{pmatrix} \tag{110}$$

5.1.4 FMR characterization via VNA detection

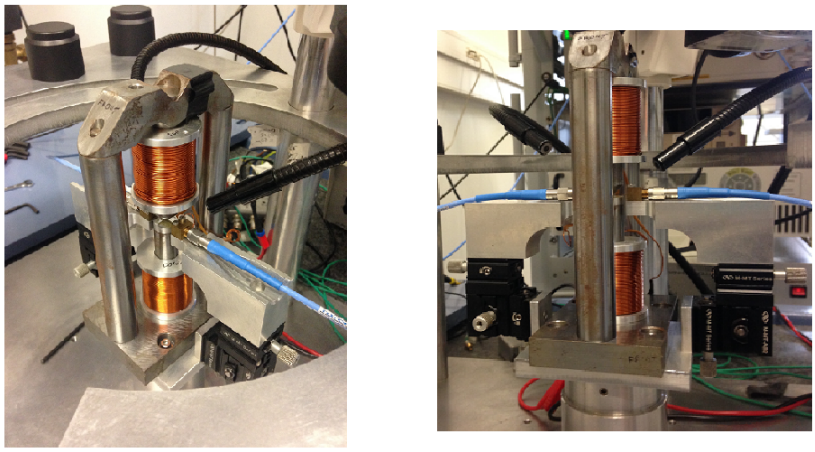

Figure 18: Picture of FMR setup in Laboratory of Magnetic Susceptibilities at IPCMS.

FMR characterization via VNA detection was performed at the laboratory of magnetic susceptibilities of Dr. Matthieu Bailleul at Institute of physics and chemistry of materials of Strasbourg(IPCMS), see figure 18. The setup consists in a 2 port VNA Agilent E8362B 10MHz-20GHz, SMA cables to transmit microwaves, picoprobes, a power supply Brüker B-AFPA 40 : ±5A 200W, a homemade resistive electromagnet (gap size 2,4 mm, pole diameter 6 mm).

We adopt the following measurement procedure. First, the coil current is set to it maximum value and then to a setpoint value, above the saturation field. This is done to ensure we follow the same hysteresis path of the electromagnet for every scan. Due to the confinment of the electromagnet gap, we cannot measure the field during the scan, therefore we proceeded to a calibarion of this electromagnet prior to study (for more details see Appendix C). Secondly, The microwave signal has an input power of $-15\ dBm$, Bandwidth = $50\ Hz$, electric delay = $0.0055\ ns$. We use low power signal to stay in linear regime response. Thirdly, we acquire data spectra by sweeping in frequency at a fixed value of field, here we perform sorth single scan (no averaging) in order to limit the possible temperature drift. As shown in figure (18), the sample lies on the pole of the electromagnet and it is thermalize with the Joule heating of the coil.

The signal in reflection is of inductive nature, an it is related with the susceptibility tensor diagonal term that we derived in section §(3.4). We measure the change of impedance between a reference field value (out of resonance) and one at resonance which gives the change of inductance defined as follows [9]:.

$$\Delta L_{nm} = \frac{1}{i\omega}[Z_{mn}(\omega, H_{res}) - Z_{mn}(\omega, H_{ref})] \tag{111}$$

Vlaminck and Bailleul [9] proposed a model of spin wave transduction that reproduce accurately the spectra in reflection and transmission. The change in the self-inductance is given by:

$$L_{11} = \frac{w\mu_o}{2\pi}\int_0^{+\infty} dk \frac{1}{k}\left|\frac{\tilde{j}_\epsilon(k,\omega)}{I}\right|^2 \frac{1}{\frac{1}{\mu_s(k,\omega,e^+)} - \frac{1}{\mu_s(k,\omega,e^-)}} \tag{112}$$

where w is the width of the strip, or the antenna, and μ_s is the surface permeability which relates the inductive field, perpendicular to the CPW, and the pumping field responsible for the dynamics:

$$\mu_s(k,\omega,z_o) = \lim_{z\leftarrow z_o} -i\frac{\tilde{b}_z(k,z,\omega)}{\mu_o \tilde{h}_x(k,z\omega)} \tag{113}$$

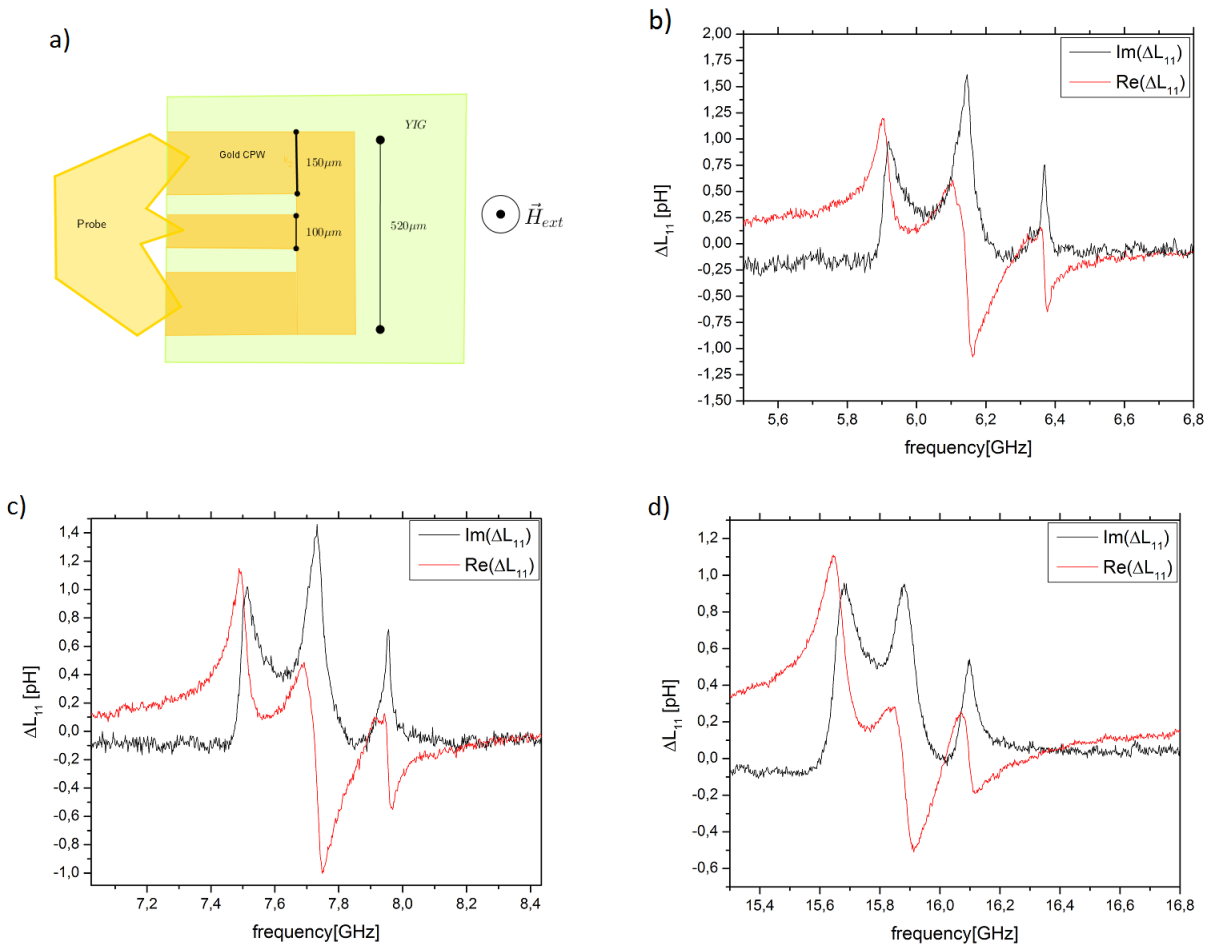

Figure 19: a) Top view of film with CPW used to perform FMR for uniform excitation. Spectra in reflection ΔL_{11} b) $\mu_o H_{ext} = 0,3507 \quad T$ b) $\mu_o H_{ext} = 0,4073 \quad T$. c) $\mu_o H_{ext} = 0,6934 \quad T$

The spectra showed in figure (19) shows the real and imaginary part of the change of induction in reflection of the port 1 in the CPW (ΔL_{11}). First, we observe that the spectra has its imaginary and real components to have a a lorentzian and derivative of a lorentzian line shape respectively. In section §(3.4), we found the susceptibility tensor, whose diagonal term deter-

mines the amplitude of precession shows the same characteristic. We can say that the change of inductance is related to the susceptibility tensor diagonal term. Secondly we observe that spectra for uniform excitation presents several peaks. This is due to inhomogeneities in the film, which comes from the difficulty to grow homogeneous thin films of YIG. The linewidth of the imaginary part is due to three main causes. First contribution, intrinsic damping of the film, $\Delta f \propto 2\alpha f$, which is clearly observed in figure (19) that the linewidth increases with frequency. Second contribution, the inhomogeneous broadening of the emission spectra, $\Delta f \propto v_g \Delta k$, considering v_g to decrease slightly with frequency makes this contribution constant. Third contribution, the inhomogeneous broadening from magnetic inhomogeneities, $\Delta f \propto \Delta H_o$, which is frequency independent. Unfortunately, we cannot analyze damping directly from the linewidth of resonance peaks, as they tend to merge for higher values of field, and the information is not accurate. Rather we extract the value of the damping, from the attenuation length of the propagation of the spin waves, which will be explained in detail in the next section.

FMR characterization with non-uniform excitation is done using a CPW with constriction, as shown in figure (20). The CPW excites MsFVW with wave vector $k = 5.9\ \mu m^{-1}$. We can observe that there is also several peaks, however these peaks correspond to different sections of the CPW, which according to the dispersion relation (91) higher frequency peaks correspond to higher wave vector. The width of the peak at higher frequency is larger than the two contributions of damping and inhomogeneous broadening of the emission spectra, Δk. This anomalous linewidth is probably due to the merging of multipeaks with magnetic inhomogeneities origin shown in uniform excitation spectra.

We summarize our spectra in figure (21), where we plotted the frequency at resonance against external field for $k = 0$ and $k_2 = 5.9\ \mu m^{-1}$. We fit the data with a simplified version of equation (91), where we take a first approximation for the term $kt \ll 1$ ($k = 5.9\ \mu m^{-1}$, $t = 0.029 \mu m$, $kt = 0.171$), we obtain the following expression:

$$\omega^2 = \gamma^2 \mu_o H_{eff} (\mu_o H_{eff} + \mu_o M_s \frac{kt}{2}) \tag{114}$$

where $H_{eff} = H_{ext} - M_{eff}$, M_s saturation magnetization, k is the wave vector determined by the width of the CPW, $t = 29nm$ is the thickness of the film, which was determined via x-ray reflectivity. The values we found are gyromagnetic ratio of $\mu_o \gamma = 27.71\ GHz/T$ and effective magnetization $\mu_o M_{eff} = 0.1291\ T$, for $k = 0$. Also, for $k = 5.9 \mu m^{-1}$ we obtained $\mu_o \gamma = 27.83\ GHz/T$ and $\mu_o M_{eff} = 0.1236\ T$. Now if we take the difference between the square of the resonance frequency for distinct k vector, as shown in figure (21) we can separate M_s from H_k:

$$|\omega^2(k = 0) - \omega^2(k = k_o)| = \gamma^2 \mu_o^2 (H_{ext} - M_{eff}) M_s \frac{k_o t}{2} \tag{115}$$

From this equation the saturation magnetization M_s appears as an independent parameter. This cannot done with just FMR measurement for one k vector. We found, $M_s = 0.153\ T$ and the

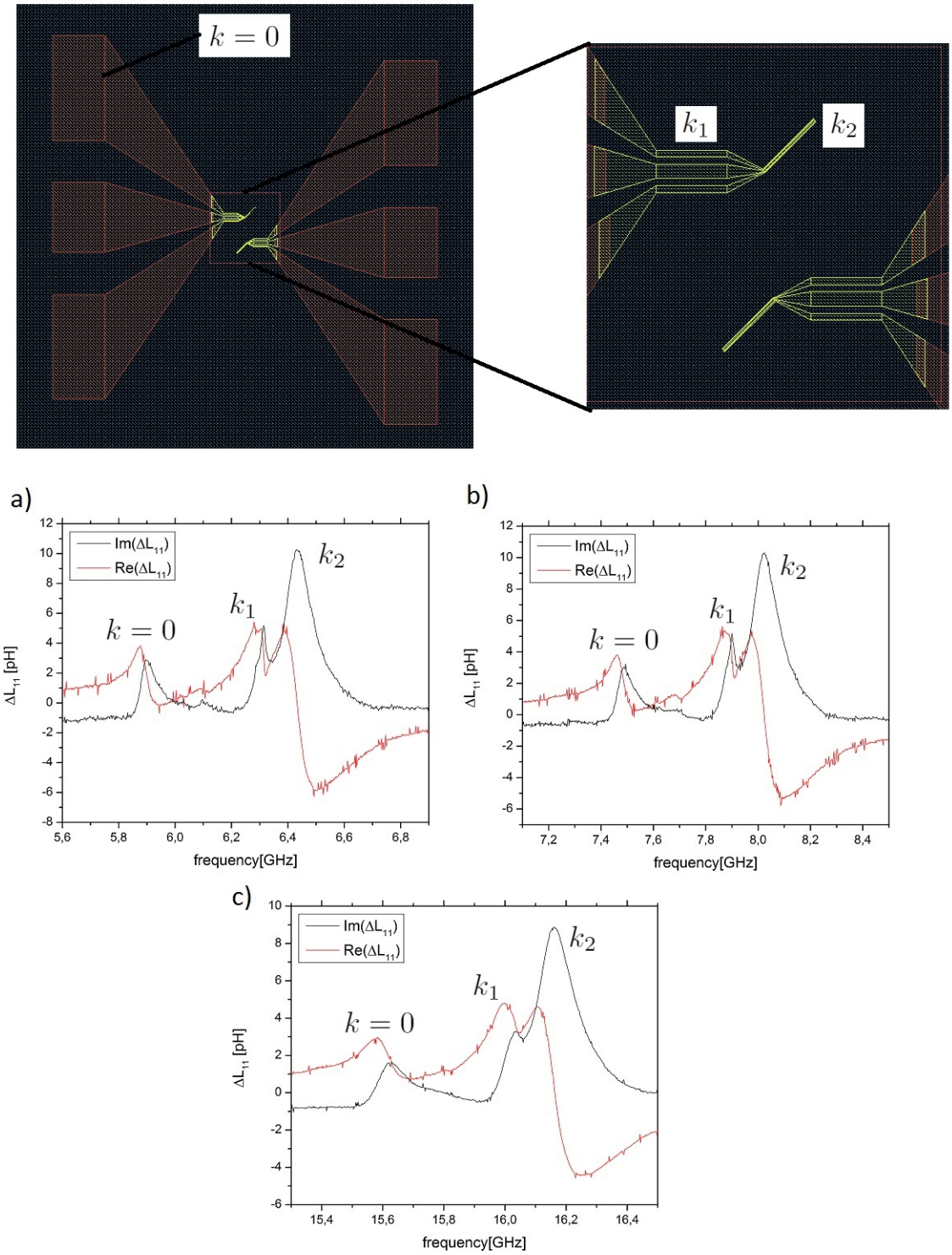

Figure 20: Spectra in reflection ΔL_{11}. This spectra correspond for non-uniform excitation for a CPW with $k_2 = 5.9\mu m^{-1}$. a) $\mu_o H_{ext} = 0.3507 \quad [T]$. b) $\mu_o H_{ext} = 0.4073 \quad [T]$ c) $\mu_o H_{ext} = 0.6123 \quad [T]$

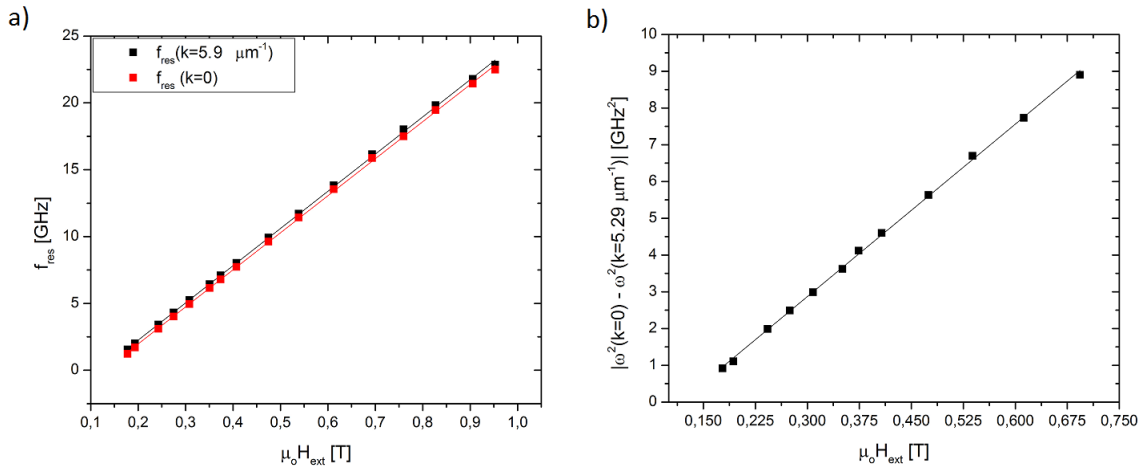

Figure 21: Fitting of Kittel formula to extract H_k, γ and M_s. a) Resonance frequency as function of external field, for $k = 0$ and $k_2 = 5.9\mu m^{-1}$. b) Difference of the square of the frequency of resonance.

uniaxial anisotropy field $\mu_o H_k = \mu_o(M_s - M_{effs}) = 0.029\,T$.

5.2 Propagating Spin Wave Spectroscopy (PSWS)

The Propagating Spin Wave Spectroscopy is a technique used to excite and detect spin waves using two pair of antennae. The first antennae works as an emitter, that generates nonuniform excitation. The propagated spin wave underneath the second antennae induces a voltage, as figure (22) shows. The second antenna is at a distance D from the first one. The VNA measures the S-parameters from which we can extract the mutual inductance between antennae ΔL_{12}. Lets consider the magnetization vector, in the case of absence of damping ($\alpha = 0$). In this case the spin wave takes the form of a plane wave $\mathbf{m}(x,t) = \mathbf{m}_o e^{i(\omega t - k_t x)}$, where ω is the microwave frequency. Assuming the antenna to be pointlike, e.g. the dimension of the antenna along the propagation direction is zero. The delay of the wave, or phase accumulation, when is detected by the other one is $\phi = -kD$ (where D is the distance between antennae), see figure (22). As the VNA sweeps the frequency a continuous range of k vectors, which cause a continuous variation of the phase for each k vector (cf. (23.c) $TF[j]$). This produce an oscillation in the envelope of the resonance peak, such as the mutual inductance spectra of figure (23.b)) shows. We also realize that the line shape of the envelop is lorentzian, and in fact has the same width as the reflection signal ($Im(\Delta L_{11})$). The spectra in transmission have two distinct characteristics that are measure: the amplitude and the period of oscillation, see figure (23(b)). From the period of oscillation f_{osc} we can estimate the group velocity of the wave v_g, which for a full period of phase accumulation, $\delta\phi = 2\pi = \delta k D$, assuming group velocity to be the same for all k vector within the main peak of the Fourier transform. we have $\delta k = 2\pi f_{osc}/v_g$, so the group velocity

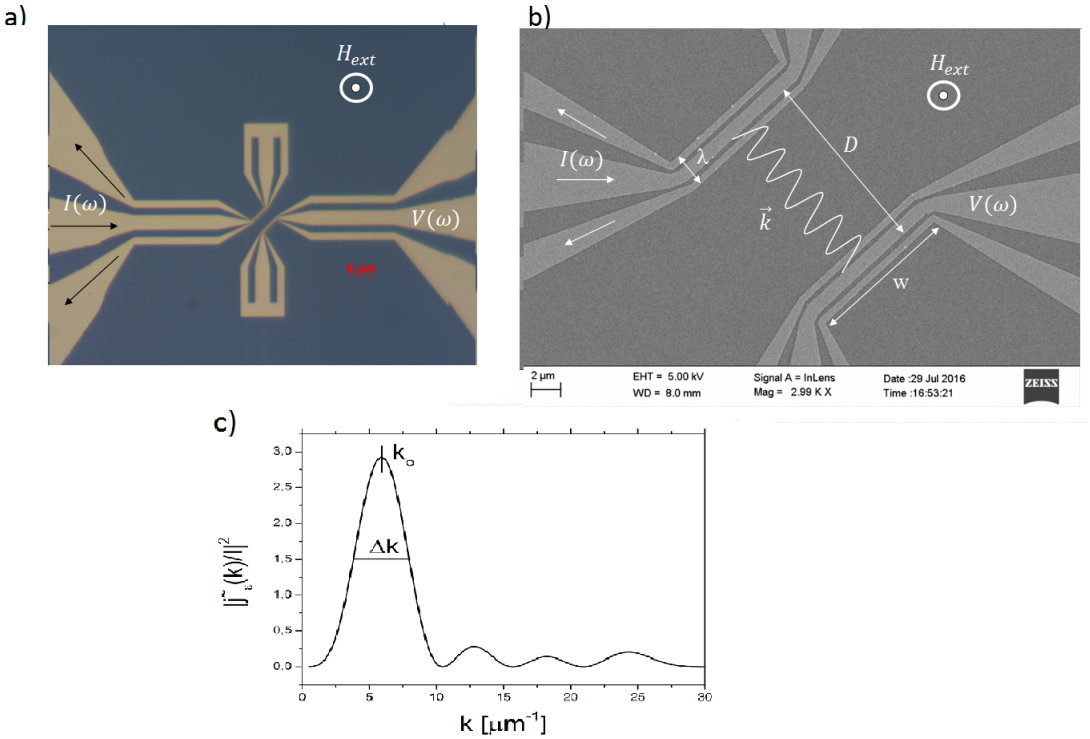

Figure 22: Pair of antennae for PSWS technique. a) Optical picture showing the direction of the current in th signal and ground lines. b) SEM picture of pair of antenna showing the dimensions of importance for the characterization of the spectra. c) Amplitude square of the current normalized Fourier Transform of the current density for the antenna, just the constriction.

is:

$$v_g = f_{osc} \cdot D \tag{116}$$

Considering now the effect of damping, attenuation causes a decrease in the amplitude of the spin wave as it travels across the film. The magnetization vector considering the damping is $\mathbf{m}(x,t) = e^{x/L_{att}} e^{i(\omega t - k_t x)}$, where L_{att} is the length at which the angle of precession has decreased a factor $1/e$. L_{att} is defined from the characteristic time of decay $\tau = 2/\alpha\Delta f$ which is defined from the inverse of half of the linewidth in the resonance peak, according to equation 41:

$$L_{att} = \tau v_g = \frac{v_g}{\alpha\omega} \tag{117}$$

We can relate the amplitude in reflection and transmission as follows:

$$\Delta L_{12} = \frac{1}{2}\Delta L_{11} e^{\frac{-D}{L_{att}}} \tag{118}$$

the factor 1/2 is due to the fact we only measure waves in one direction $k > 0$. Evidently this approximation of pointlike antenna is not enough to understand spectra when D and L_{att} are comparable to the extension of the antenna. Vlaminck and Bailleul [9] proposed an electromag-

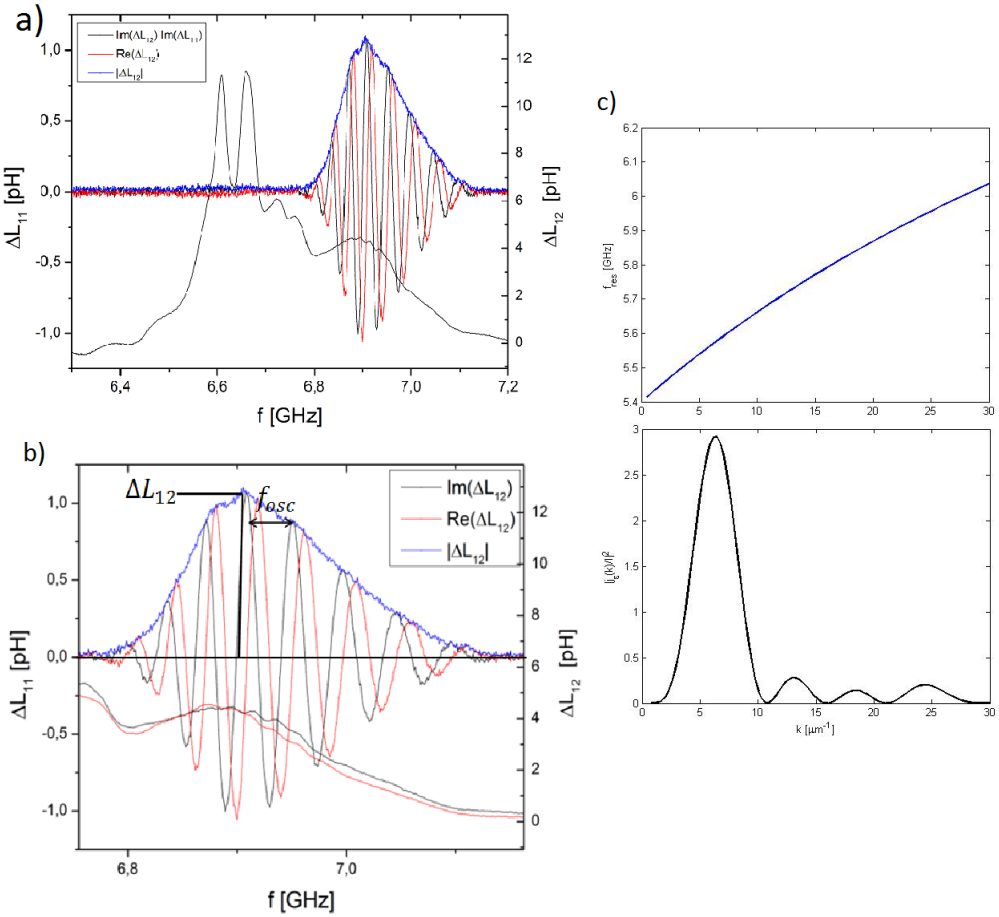

Figure 23: a) spectra in reflection and transmission, ΔL_{11} and $\Delta L12$. b) Spectra in transmission, the f_{osc} is the frequency difference of two adjacent peaks. c) dispersion relation for MFVW's with $\mu_o H_{eff} = 0.2T$ and $\mu_o M_s = 0.15T$, d) Fourier transform of a CPW for $\lambda = 1\mu m$

netic model that describes the transduction of spin waves between antennae. They obtained the following expression for the mutual inductance:

$$L_{12} = \frac{w\mu_o}{2\pi}\int_0^{+\infty} dk \frac{e^{-ikD}}{k}\left|\frac{\tilde{j}_\epsilon(k,\omega)}{I}\right|^2 \frac{1}{\frac{1}{\mu_s(k,\omega,e^+)} - \frac{1}{\mu_s(k,\omega,e^-)}} \tag{119}$$

where w is the width of the strip, or the antenna, and μ_s is the surface permeability which relates the inductive field, perpendicular to the CPW, and the pumping filed responsible of the dynamics:

$$\mu_s(k,\omega,z_o) = \lim_{z\leftarrow z_o} -i\frac{\tilde{b}_z(k,z,\omega)}{\mu_o \tilde{h}_x(k,z,\omega)} \tag{120}$$

6 Antennae Design

6.1 Fresnel Diffraction

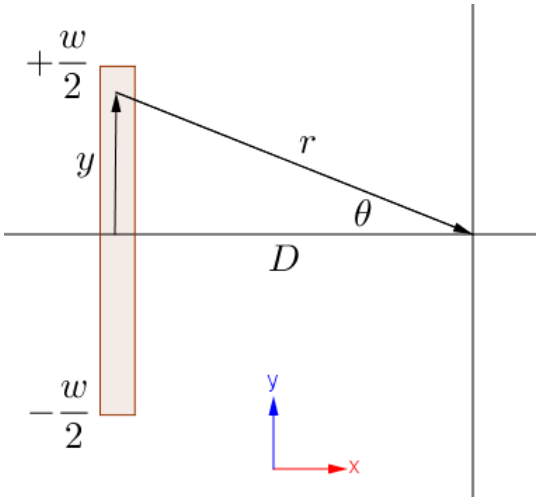

Figure 24: Geometry of an antennae emitting spherical waves to measure the intensity at a perpendicular plane to the antenna at distance D.

In this section we propose to describe the spin wave generation of a finite element of a CPW in terms of Fresnel near-field Diffraction phenomena. First we have to do the assumption, that each point of the antenna is a source of circular waves, in all directions. Also, that the distance is larger than the width of the line, $\sim 1\mu m$. This problem can be seen as diffraction of plane waves by a slit of size w. We can write the differential element of the wave as follows:

$$dS = \frac{S_o}{\sqrt{r\lambda}} \cos(kr - \omega t) \tag{121}$$

where S is the amplitude of the wave, r the distance from the source to the point where measure the amplitude, $k = 2\pi/\lambda$ the wave vector[11]. Spin waves have properties that EM waves in vacuum does not have, in particular the magnetostatic surface waves has an anisotropic dispersion relation, However, in the case of out of plane magnetostatic forward volume waves does not have any anisotropy. Also, spin waves present an exponential attenuation. Averaging over time, and taking the square of the amplitude to measure the intensity of wave in the perpendicular plane at distance D we obtain the following expression:

$$\begin{aligned} I(s) = \left(\frac{I_o}{2\lambda}\right)^2 [&\int_{-w/2+s}^{w/2+s} \frac{1}{\sqrt{r}} e^{-r/L_{att}} e^{ikr} dy \\ &- \int_{-w/2+s}^{w/2+s} \frac{1}{\sqrt{r_-}} e^{-r_-/L_{att}} e^{ikr_-} dy \\ &- \int_{-w/2+s}^{w/2+s} \frac{1}{\sqrt{r_+}} e^{-r_+/L_{att}} e^{ikr_+} dy]^2 \end{aligned} \tag{122}$$

with I_o the intensity of the incident wave at the slit, in this case the signal in reflection, L_{att} the attenuation length, $r = \sqrt{D^2 + y^2}$, $r_- = \sqrt{(D - \lambda/2)^2 + y^2}$, $r_+ = \sqrt{(D + \lambda/2)^2 + y^2}$ [11]. The three integrals represent the central line, signal line, and the two ground lines with a minus sign. Each point of amplitude is an integral to solve, to obtain all the points we move the slit, being the same as shifting the point of measurement. We performed simulations obtaining the following amplitude profiles.

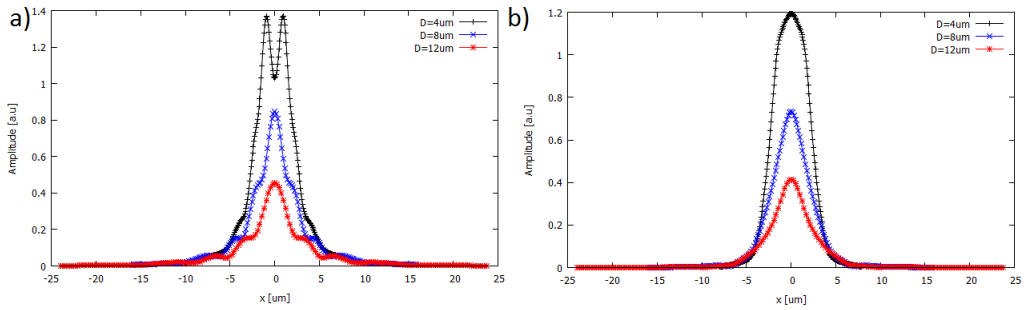

Figure 25: Amplitude profile of an spin wave measured at distinct distances, a) $\lambda = 1\mu m$, $L_{att} = 7\ \mu m$ and $w = 5\mu m$ b) $\lambda = 1\mu m$, $L_{att} = 7\ \mu m$ and $w = 5\mu m$, averaging with the probe size $w = 2\ \mu m$

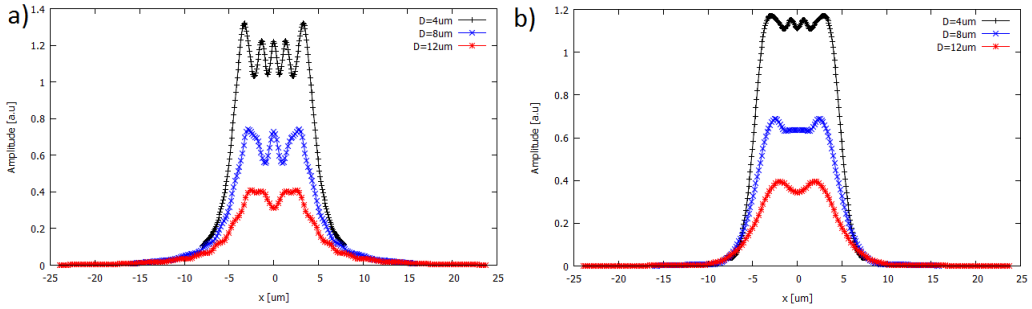

Figure 26: Amplitude profile of an spin wave measured at distinct distances, a) $\lambda = 1\mu m$, $L_{att} = 7\ \mu m$ and $w = 10\mu m$ b) $\lambda = 1\mu m$, $L_{att} = 7\ \mu m$ and $w = 10\mu m$, averaging with the probe size $w = 2\ \mu m$

From figure (25) we can see that the amplitude of the wave decrease to almost zero at shifts greater that the width of the antennae. The intensity show oscillations in its value which is characteristic of diffraction patterns. The introduction of attenuation factor introduce a decrease of the intensity and increases number of oscillations. The simulations show that an antennae with a finite width does not excite a beam but is the diffraction that produce it. We only need finite length antennae, with k vector large enough to separate from the rest CPW, the peaks of the Fourier transform should be well separated.

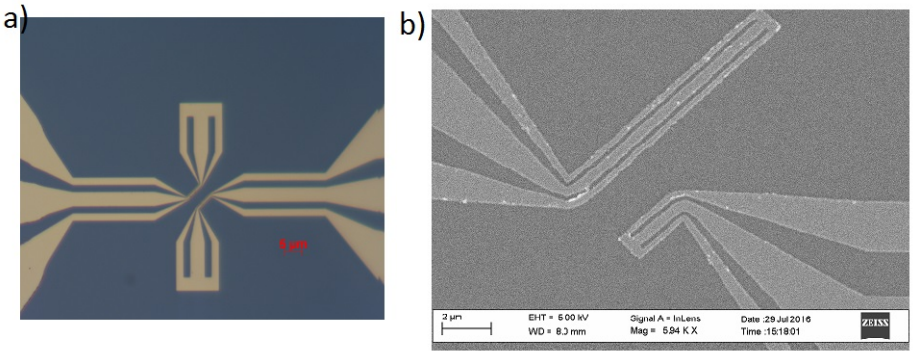

Figure 27: a) Optical image of developed film after lithography of antenna with continuous constriction, Geometry No. 1. $w = 5\mu m$, $\lambda = 1\mu m$, $D = 4\mu m$ b) SEM image of device of antenna with sudden extreme bend and end shorted, Geometry No. 2. $w5\mu m$, $\lambda = 1\mu m$, $D = 4\mu m$, Mapping device shift $s = -4\mu m$

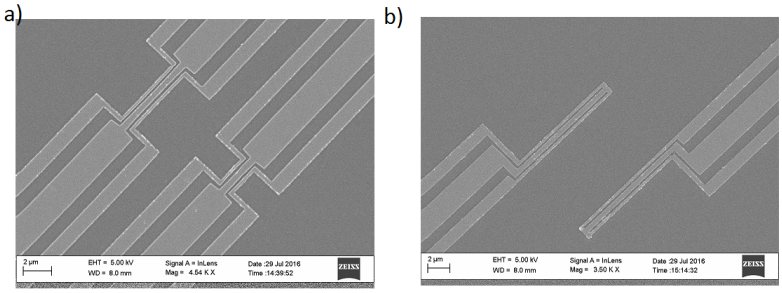

Figure 28: a) SEM image of antenna with sudden constriction, Geometry No. 3. $w = 5\mu m$, $\lambda = 1\mu m$, $D = 4\mu m$ b) SEM image of the device of antenna with sudden constriction and end shorted, Geometry No. 4. $w = 10\mu m$, $\lambda = 1.2\mu m$, $D = 8\mu m$

6.2 Fabricated Antennae

Various Geometries were designed to explore distinct aspects of the spin waves, such as: attenuation lengths, velocity, focusing of the beam and mapping of amplitude of the spin wave. The different geometries explored are listed below:

- Antennae with continuous constriction, Geometry No. 1, figure (27).
- Antennae with sudden ”extreme” bend and end shorted, Geometry No. 2, figure (27).
- Antennae with sudden constriction, Geometry No. 3, figure (28).
- Antennae with sudden constriction and end shorted, Geometry No. 4, figure (28).
- Antennae for Ferromagnetic Resonance, figure (29).

Different antennae were fabricated to explore the spectra of transmission. In the case of mapping devices, figures (27,30), we designed a pair of antennae, with a receiver smaller than the emitter. Each mapping device is fabricated with the receiver at distinct shifts and distances

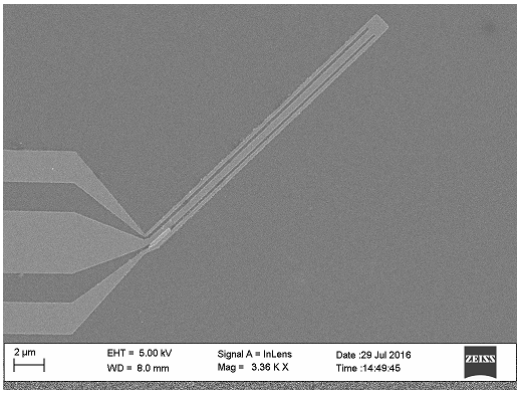

Figure 29: FMR device. SEM image of the device, $w = 20\mu m$, $\lambda = 1\mu m$

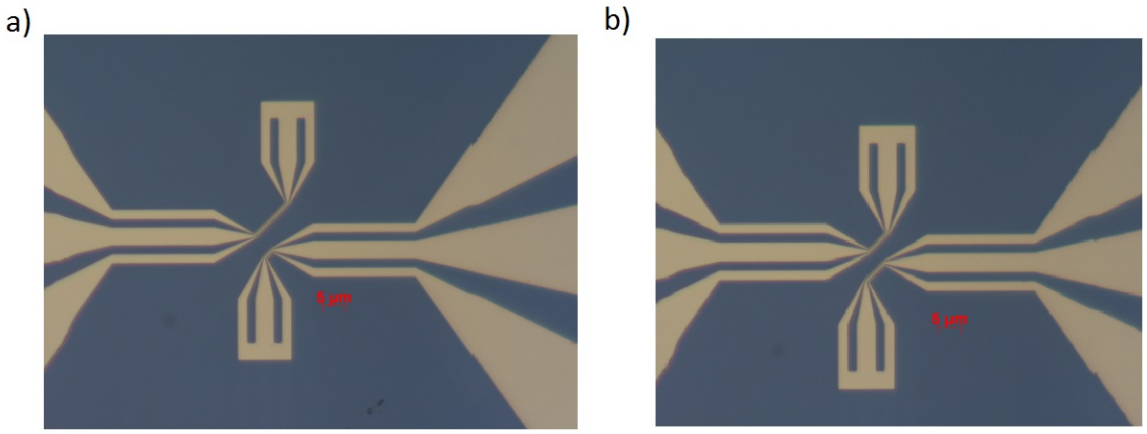

Figure 30: a) Optical image of developed film after lithography of antenna with continuous constriction, Geometry No. 1. Mapping device, Receiver shifted $5 = \mu m.$, constriction length of emitter $10\mu m$, width of receiver $w = 2\mu m$, $\lambda = 1.2\mu m$, $D = 5\mu m$ b) Optical image of developed film after lithography of Antenna with continuous constriction, Geometry No. 1. same length constriction, shifted one respect to other. Receiver shifted $5 = \mu m$, constriction width $5\mu m$, $\lambda = 1\mu m$, $D = 4\mu m$

respect to the emitter, in order to have a discrete mapping of the spin wave amplitude in $x - y$ plane. We fabricated mapping devices only for geometries No. 1 and No. 2. We also fabricated identical antennae to measure focusing of the beam, antennae are shifted. We fabricated equal size antennae with shift for Geometry No. 1, see figure (30). For all geometries, we fabricated pair identical of antennae with different and width to estimate attenuation lengths, see figure (27). We summarize all devices fabricated with their dimensions in the following table:

1st Batch										
Geometry No. 1	Same size $\lambda = 1$ µm w=5 µm	D [µm]		Same size shifted $\lambda = 1$ µm w=5 µm	D [µm]			mapping devices $\lambda = 1$ µm D = 5 µm w=5 µm	s [µm]	
		4	√		4	s=0.5	√		0	√
		6	√			s=1	√		1	√
		8	√			s=1.5	√		2	√
		10	√		10	s=0.5	√		3	√
		12	√			s=1	√		4	√
		14	x			s=1.5	√		6	√
	Same size $\lambda = 2$ µm	D [µm]		Same size shifted $\lambda = 2$ µm	D [µm]			mapping devices $\lambda = 2$ µm D = 10 µm	s [µm]	
		5	x		5	s=0.5	√		0	x
		7,5	√			s=1	√		2	√
		10	x			s=1.5	√		4	√
		12,5	√		12,5	s=0.5	√		6	√
		15	√			s=1	√		8	x
		17,5	x			s=1.5	√		12	√

2nd Batch							
FMR devices	$\lambda = 0{,}5$ µm						
	$\lambda = 1$ µm						
	$\lambda = 10$ µm						
	$\lambda = \infty$						
Geometry No. 1		D = 4 [µm]		D = 8 [µm]		D = 12 [µm]	
	Same size $\lambda = 1$ µm	w = 0 [µm]	√	w = 0 [µm]	√	w = 0 [µm]	√
		w = 2 [µm]	√	w = 2 [µm]	√	w = 2 [µm]	√
		w = 5 [µm]	√	w = 5 [µm]	√	w = 5 [µm]	√
		w = 10 [µm]	√	w = 10 [µm]	√	w = 10 [µm]	√
Geometry No. 2		D = 4 [µm]		D = 8 [µm]		D = 12 [µm]	
	Same size $\lambda = 1$ µm	w = 0 [µm]	√	w = 0 [µm]	√	w = 0 [µm]	√
		w = 2 [µm]	√	w = 2 [µm]	√	w = 2 [µm]	√
		w = 5 [µm]	√	w = 5 [µm]	√	w = 5 [µm]	√
		w = 10 [µm]	√	w = 10 [µm]	x	w = 10 [µm]	√
	mapping devices $\lambda = 1$ µm	D = 4 [µm]		D = 8 [µm]		D = 12 [µm]	
		s = 0 [µm]	x	s = 0 [µm]	√	s = 0 [µm]	√
		s = 2 [µm]	√	s = 2 [µm]	√	s = 2 [µm]	√
		s = -2 [µm]	√	s = -2 [µm]	√	s = -2 [µm]	√
		s = 4 [µm]	√	s = 4 [µm]	√	s = 4 [µm]	x
		s = -4 [µm]	√	s = -4 [µm]	√	s = -4 [µm]	√
		s = 6 [µm]	√	s = 6 [µm]	√	s = 6 [µm]	√
		s = -6 [µm]	√	s = -6 [µm]	√	s = -6 [µm]	x
		s = 8 [µm]	√	s = 8 [µm]	√	s = 8 [µm]	√
		s = -8 [µm]	√	s = -8 [µm]	√	s = -8 [µm]	x
Geometry No. 3		D = 8 [µm]					
	Same size $\lambda = 1$ µm	w = 0 [µm]	√				
		w = 5 [µm]	√				
		w = 10 [µm]	√				
Geometry No. 4		D = 8 [µm]		D = 12 [µm]			
	Same size $\lambda = 1$ µm	w = 2 [µm]	√	w = 2 [µm]	√		
		w = 5 [µm]	√	w = 5 [µm]	√		
		w = 10 [µm]	√				

Figure 31: Summary of all devices fabricated, working devices (✓), no working devices (x)

7 Fabrication Process

The devices used to excite the spin wave beam, discussed in section §(7.2), were fabricated using electron beam lithography and gold deposition over the same films of YIG(Yttrium Iron Garnet). In this section we will present the fabrication process of the antennae used to detect a spin wave beam.

7.1 Electron Beam Lithography

Electron beam lithography uses a beam of high energy electrons ($20\ kV$) to draw nanometric size pattern on to polymer resin film Polymethyl methacrylate (PMMA). However, one cannot pattern directly via e-beam lithography on an insulating substrate using only PMMA resin, as the charge of the e-beam would accumulate in a wide region of the sample. To circumvent this problem we spin coated on top of the PMMA layer, a layer of conductive resin (SXAR-PL5000/90.2) which allows for the charge to be evacuated (See appendix D for the details of the sample preparation). However, the success rate using this conductive resin compared with PMMA on Si wafer are much lower, making it very difficult to achieve fine line of $100\ nm$ width.

7.1.1 Mask Pattern

The devices were designed using Layout editor CAD software to create masks with nanometric precision. Each Mask has two parts, the contact pads to land the probes, and the antenna which correspond to the small feature size. The size of the contacts fits in a square of $1000\mu m$ with spacing of the probe pitch of $150\mu m$. The antennae fits in a square of $100\mu m$, See figure (32).

7.1.2 Lithography

The lithography process was done at the Institute of Physics and Chemistry of the materials in Strasbourg (IPCMS), and ST-NANO facilities. We use an electron beam microscope Zeiss Supra 40, with nanolithography Raith electronics, figure (33).

Given that the device needs different magnification for the outer and inner parts lithography process was done in two steps. At the higher magnification we exposed the antennae, which corresponds to the smallest feature size (figure (32(b))), and at the lower magnification we exposed the probes contact pads (figure (32(a))). When we change magnification, the aperture of the beam is also changed, therefore a deflection of the beam occurs. A compensation between each step in implemented to compensate the deflection of the beam. Parameters were chosen after doing a dose test on Silica wafers and YIG films. A dose test is the exposition of different patterns with increasing dose to control the dose which fits the best with the desired pattern, see table (1).

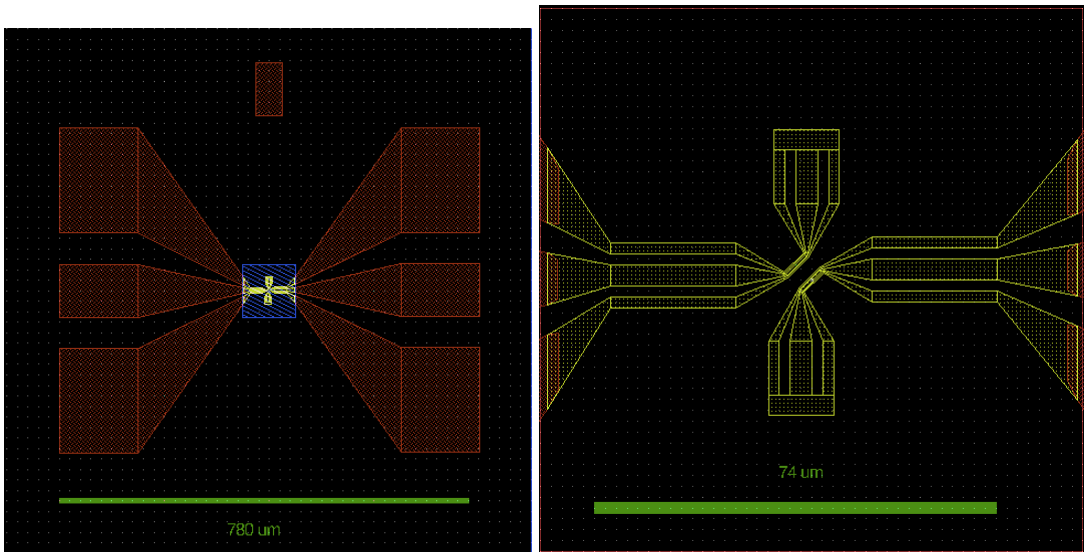

(a) Device showing probes contacts (b) Antenna

Figure 32: Mask for antenna, Distance $4\mu m$, Width of antenna $1.2\mu m$, length of antenna $5\mu m$.

Figure 33: Zeiss Supra 40 electron beam microscope at IPCMS.

The next step after exposition is to remove the conductive resin and develop the PMMA, that was exposed in the lithography process, with a commercial solvent. The film has the pattern dug in the PMMA resin, after which sample is ready to transfer the pattern with a gold lift-off.

7.2 Metal Deposition

We transferred the pattern on to the film with gold lift-off. We use an electron beam evaporator chamber, Plassys MEB550S, at the clear room of the IPCMS, see figure (34. a)). Electron beam evaporation use a beam of thermal electrons, which are focused with a magnetic field to evaporate the metal in way we obtain a focus source of atoms to be deposited on the film, see figure (34. b)). We deposited successively adhesive layer of Titanium , $\sim 5nm$, followed by 80 nm of Gold. This technique has the advantage to produce a punctual source of evaporation

Stage	Magnification	Aperture of Gun (μm)	Current (nA)	Dose ($\mu C/cm^2$)
1	60	10	0.02506	175 ± 10
2	600	120	3.9155	250 ± 30

Table 1: Setting parameters for the lithography process.

which is critical for the quality of the lift off. Later, we introduce the film, for several hours, in acetone to then proceed to lift the excess of gold.

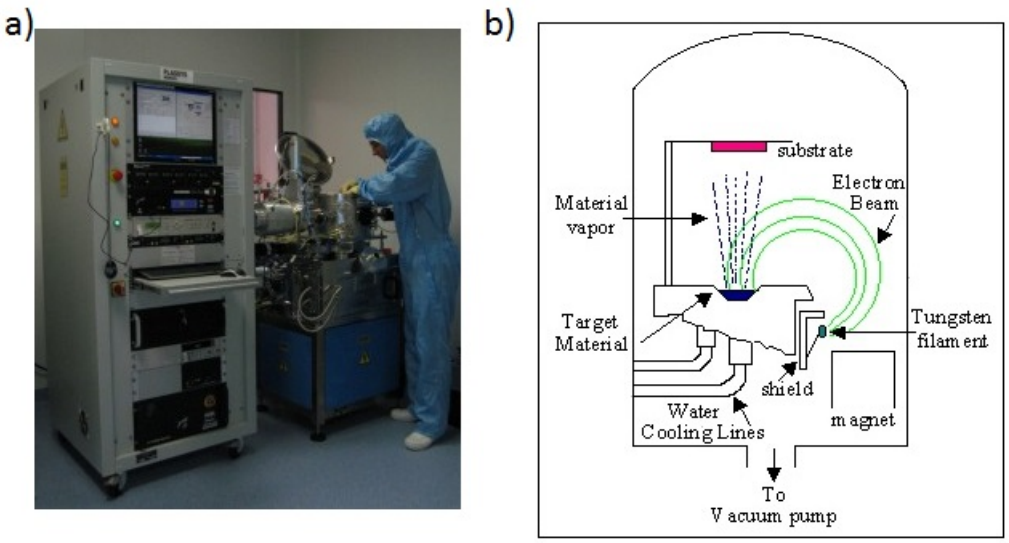

Figure 34: a) Plassys MEB550S electron beam evaporator at IPCMS. b) E-beam evaporation process. A beam of electrons is guided with a magnetic field, the beam hits the metal source and evaporates metal which ascends and is deposited on the film. The rate of deposition is controlled with a quartz detector.

8 Results

We present here three different tests to determine the degree of focusing of the spin wave emitted from a constriction. In a first batch of antennae we vary the distance between D, to determine attenuation lengths. In a second batch, we varies the shift of identical antennae of Geometry No. 1, and in a third batch, we measure a series of mapping devices varying distances and shifts.

8.1 Attenuation Length

First, we start focussing the attenuation length and the group velocity for YIG for several resonance frequencies. We followed the measurement procedure explained in section §(5.1.2). We use low power input to stay in linear regime. We use bandwidth = 50 Hz, to have an optimal ratio between low noise and fast measurements. We mention already, the most important source of drift is the joule heating of the electromagnet, which heats the sample as it is placed on the pole. To limit this issue, we performed single scans, with no averaging and 1601 points. The averaging allos to reduce the signal to noise ratio to see satellite peaks, but it does not show reproducible scans. We measured a set of devices of Geometry No. 1, see figure (35), with $\lambda = 1\mu m$, $w = 5\mu m$ $D = \{4, 6, 8, 10, 12, 14\}\mu m$, and $\lambda = 2\mu m$, $w = 10\mu m$ $D = \{5, 7.5, 10, 12.5, 15, 17.5\}\mu m$, where λ is the wavelength, w is the width of the antennae and D the distance between them. We present typical spectra in transmission in figure (36).

We summarize our analysis for each field values by plotting respectively, see figure (37), $\ln|\Delta_{12}|(D)$ and $1/f_{osc}(D)$, after which a linear regression gives us direclty the attenuation lengths L_{att} and the group velocity, according to equations (117) and (115). We find in particular for antennae with wave length of $\lambda = 1\ \mu m$, an attenuation length ranging $L_{att} = \{20.7...4.1\}\mu m$ and a group velocity ranging $v_g = \{227...257\}m/s$ for frequencies between $f = \{1.5...11\}GHz$. We also found for antennae with wave length of $\lambda = 2\ \mu m$, an attenuation length ranging $L_{att} = \{11.4...3.9\}\mu m$ and a group velocity $v_g = \{185...205\}m/s$ for the range of frequencies $f = \{1.7...7.8\}GHz$. Finally, we can estimate the effective damping that accounts for the inhomogeneous broadening Δk, according to equation (118). We plotted $v_g/L_{att}(f)$, see figure (37), where we observe a clear linear dependence whose slope gives us the effective damping. We obtain a value of effective damping $\alpha = (8.5 \pm 0.2) \times 10^{-4}$ for wave length of $\lambda = 1\ \mu m$, and for wave lenght of $\lambda = 2\ \mu m$ an effective damping of $\alpha = (1.04 \pm 0.06) \times 10^{-3}$. This value of damping confirms a sufficient homogeneity within the length scale of the constriction for a discrete mapping, which allows to compare the amplitude at distinct parts of the film.

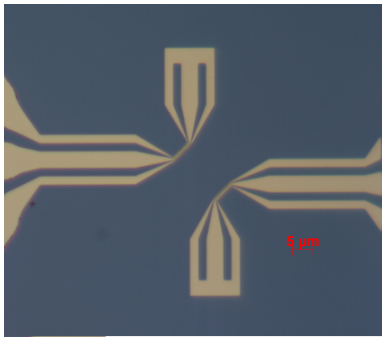

Figure 35: Optical image of developed film after lithography of antenna with continuous constriction, Geometry No. 1. $w = 5\mu m$, $\lambda = 1\mu m$, $D = 14\mu m$.

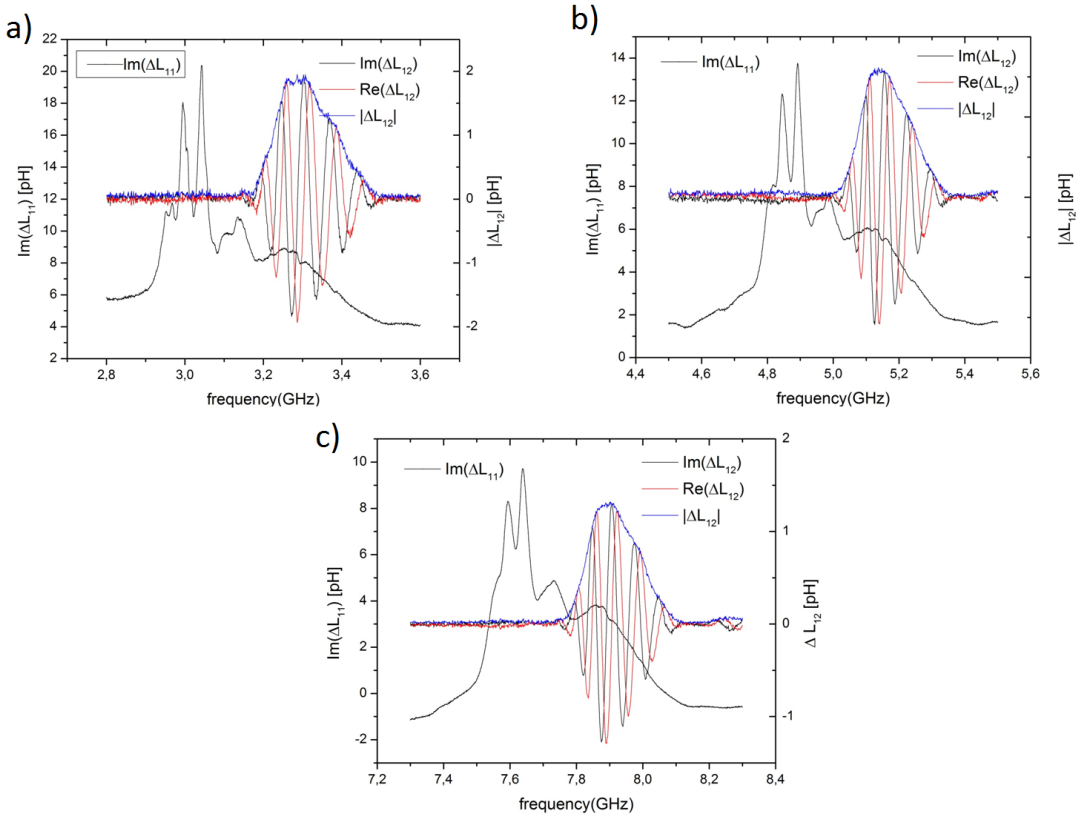

Figure 36: Spectra in transmission $|\Delta L_{12}|$, real and imaginary part, Geometry No. 1 $w = 5\mu m$, $\lambda = 1\mu m$ and $D = 4\mu m$. a) $\mu_o H_{ext} = 0,2427T$. b) $\mu_o H_{ext} = 0,3082T$. c) $\mu_o H_{ext} = 0,4073T$

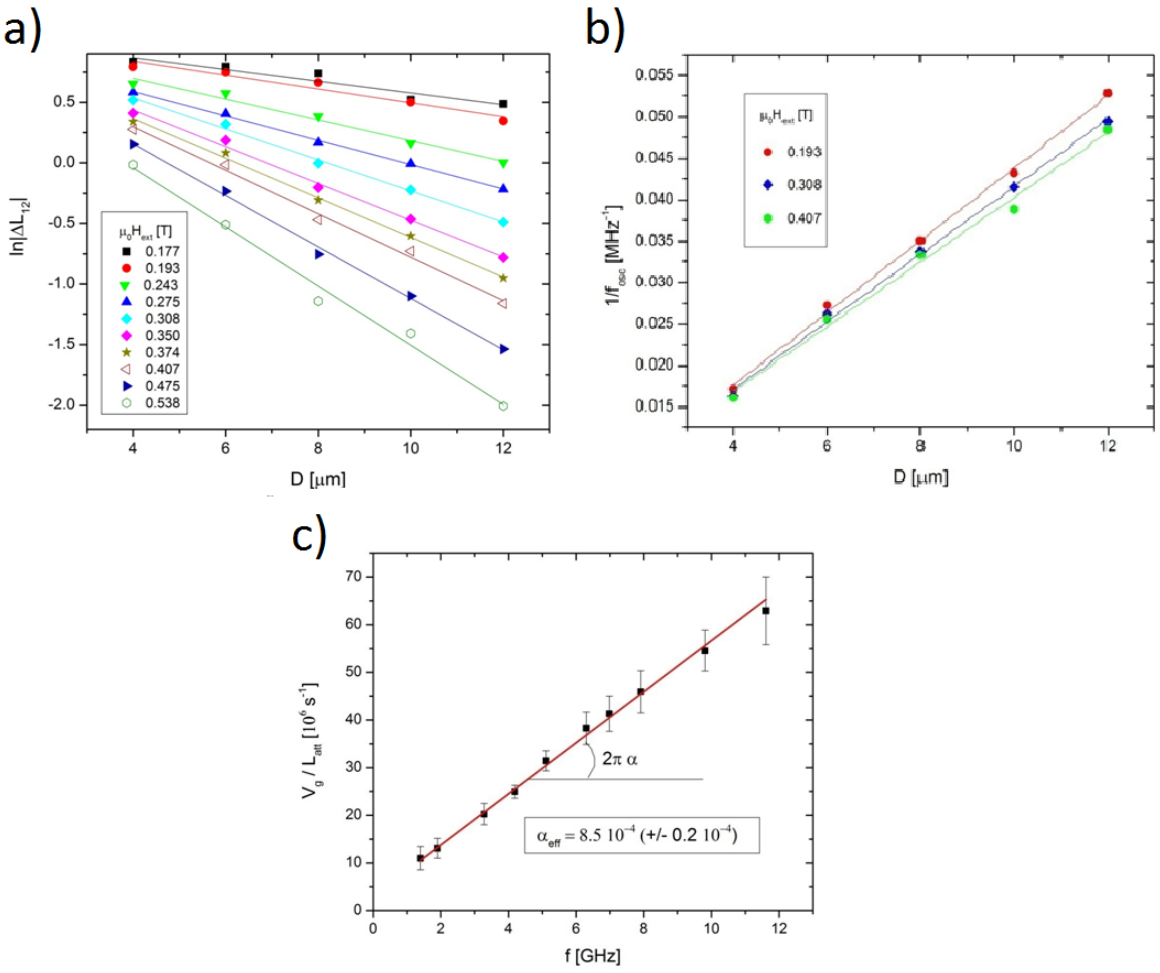

Figure 37: Antennae with $\lambda = 1\mu m$ a) $\ln|\Delta L_{12}|$ vs. D, to obtain L_{att} b) f_{osc}^{-1} vs. D, to obtain v_g. c) frequency vs. v_g/L_{att}, to obtain effective Damping.

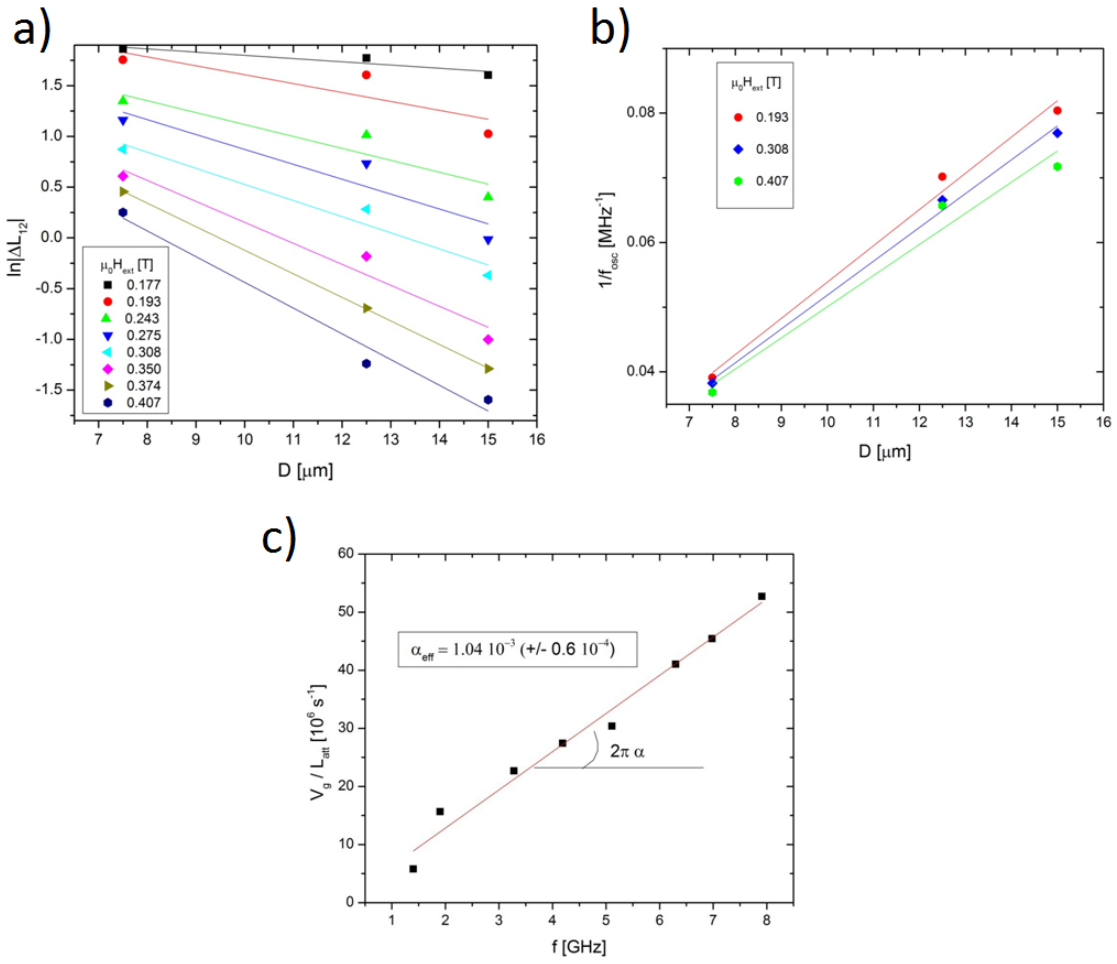

Figure 38: Antennae with $\lambda = 2\mu m$ a) $\ln|\Delta L_{12}|$ vs. D, to obtain L_{att} b) f_{osc}^{-1} vs. D, to obtain v_g. c) frequency vs. v_g/L_{att}, to obtain effective Damping.

8.2 Focusing: same size shifted antennae

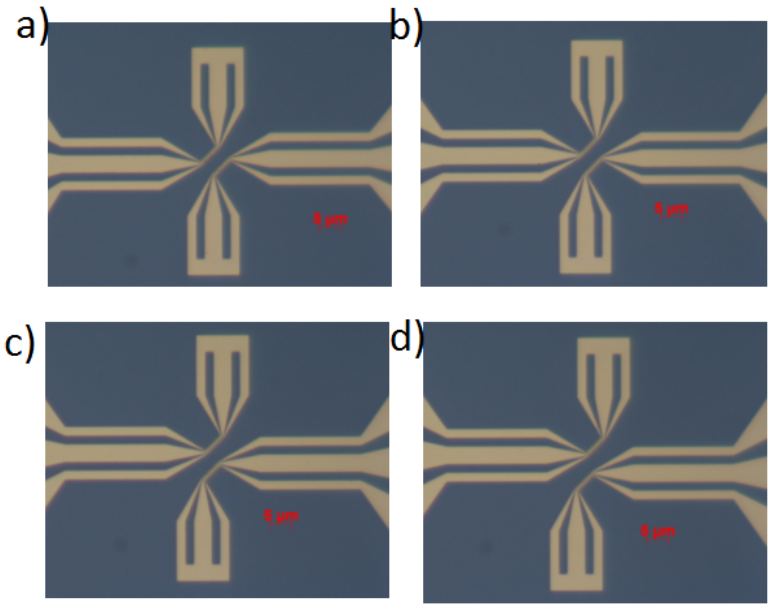

Figure 39: Antennae with $\lambda = 1\mu m$, $w = 5\mu m$ and $D = 4\mu m$ a) s=0w b) s=0.5w c) s=1w d) s=1.5w

We studied a series of devices with same size antennae shifted with respect to the other, figure (39). The shifts are measured in terms of the size of the antenna, $s = \{0, 0.5, 1, 1.5\}w$, for two distinct distances, $D = \{4, 10\}\mu m$. The amplitude in transmission is compared for the same external field and different shifts. The value of the frequency was normalized to compare the spectra, because inhomogeneities in the film produces distinct resonance frequencies (with a dispersion of maximum $300\ MHz$) for different devices, without affecting significantly the integrity and the amplitude of the spectra. In figure (40) and (41), we plotted the amplitude of the mutual inductance ΔL_{12} for all 4 devices for three distinct values of field, respectively for distances $D = 4\ \mu m$ and $D = 10\ \mu m$. The spectra shows a decrease of amplitude with shift. Namely, the amplitude is almost reduced by a factor 2 with the antennae shifted by a factor 1/2, and goes to practically to 0 for antennae completely shift. The residual signal in the case of completely shifted antennae can be understood as a crosstalk between the constricted region and the continuously enlarging section (e.g. overlap of the $|\tilde{j}_\varepsilon/I|^2$ between each section). Furthermore, one notice that the peak is shifted toward lower frequency corresponding to a transmission of lower wave vector.

Even though the amplitude does no decrease in a factor proportional to the shift, this can be caused by the continuous constriction that certainly excite spin waves with k vectors small enough to be detected by the secondary antenna. This also explains that the transmission signal for $s = 1$ and $s = 1.5$ has its peak for lower frequency than $s = 0$, the continuous constriction has k vector greater than the antenna which excites spin waves with lower frequency.

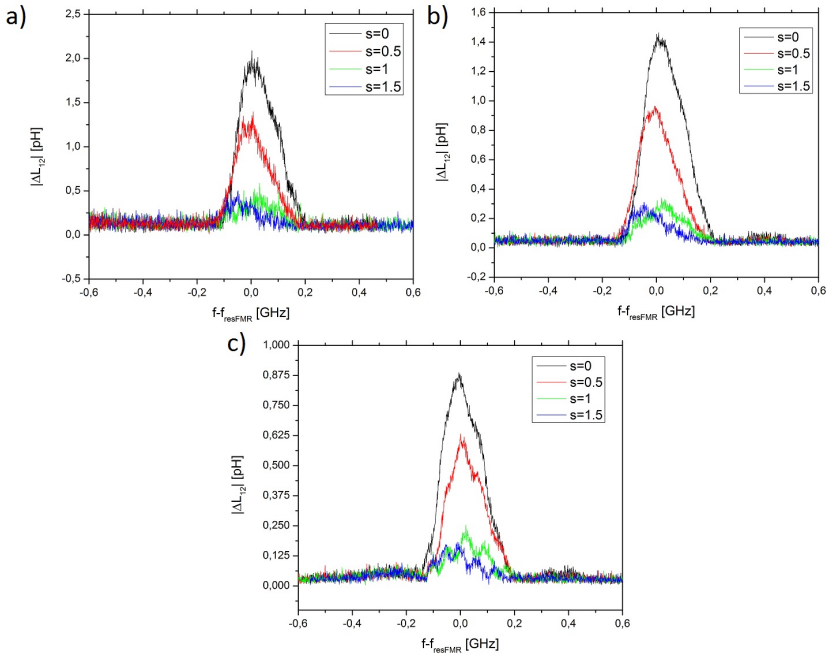

Figure 40: Amplitude in transmission $|\Delta L_{12}|$ vs. normalized frequency, for same size antennae shifted, $D = 4\mu m$. a) $\mu_o H_{ext} = 0.2427T$ b) $\mu_o H_{ext} = 0.3082T$ c) $\mu_o H_{ext} = 0.3741T$

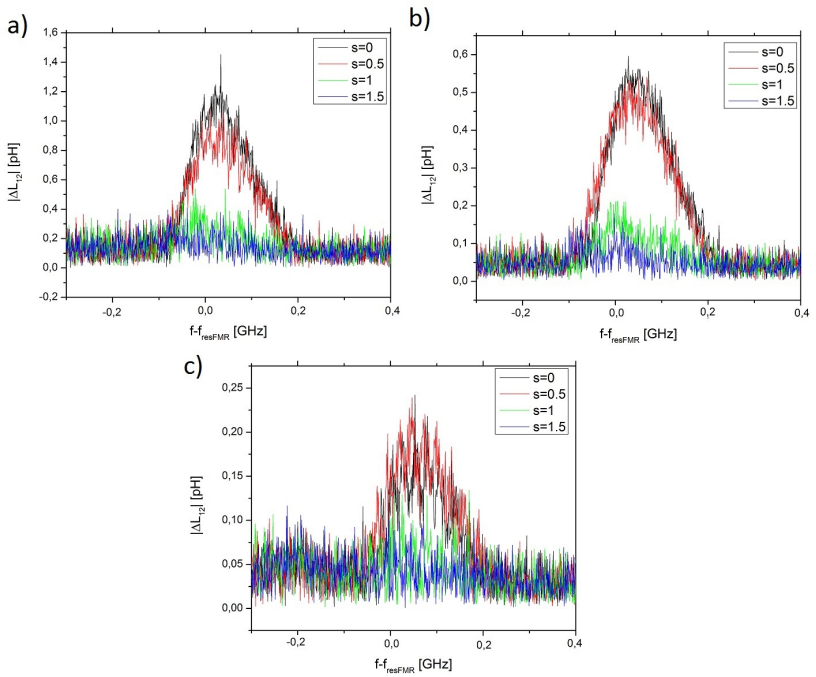

Figure 41: Amplitude in transmission $|\Delta L_{12}|$ vs. normalized frequency, for same size antennae shifted, $D = 10\mu m$. a) $\mu_o H_{ext} = 0.2427T$ b) $\mu_o H_{ext} = 0.3082T$ c) $\mu_o H_{ext} = 0.3741T$

8.3 Mapping

We then study the amplitude profile of the spin wave with mapping devices for which the probe (receiver antenna) than the emitter antenna have widths of $w_{receiver} = 2\ \mu m$ $w_{emitter} = 10\ \mu m$.

Mapping devices are fabricated with receiver a different distances and shifts respect to the emitter. This test has two purposes, first, determine the focusing of the beam and secondly measure amplitude at different points within the constriction to compare with diffraction pattern given by Fresnel near-field diffraction theory discussed in the section §(7.1). We fabricated mapping devices for Geometry No. 1 and No. 2. In figure (43), we show spectra for two mapping devices with shifts $s = 0 : \mu m$ and $s = 6\ \mu m$ respectively. We first observe that the self-inductance ΔL_{11} of the emitter stronger than the one of the receiver by a factor proportional to the ratio w_r/w_e as expected. For geometry No. 1, we measured amplitude with the receiver at $D = 5\mu m$ and $s = \{0, 1, 2, 3, 4, 6\}\mu m$, given that the antenna is symmetric we only mapped in one direction, figure (44).

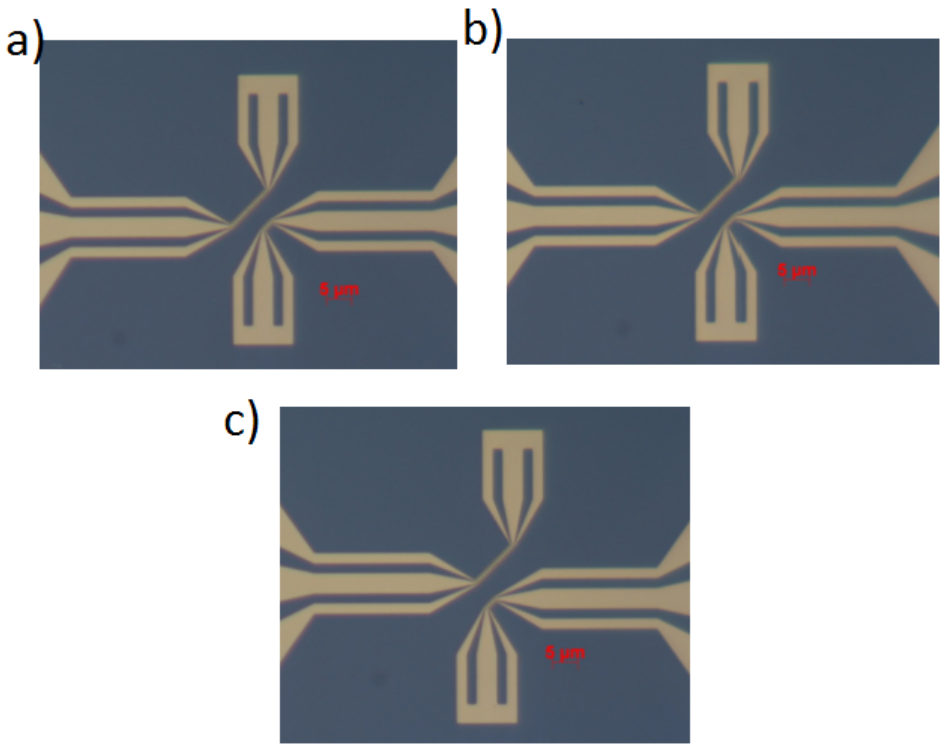

Figure 42: Mapping devices. Emitter $w = 10\mu m$ and Receiver $w = 2\mu m$, both with $\lambda = 1\mu m$ a) $s = 2\mu m$ b) $s = 3\mu m$

We summarize the amplitude of the mutual inductance ΔL_{12} in figure (44). Firstly, we observe a decrease of the amplitude as the probe is outside of the region of the constriction, although is not zero. This suggest a relatively well focused beam of size comparable to the constriction, with small residual transmission. This can be seen in the spectra for antennae shifted by $s = 6\mu m$ in figure (43), which shows that the transmission signal has lower frequency of resonance and also less oscillations than $s = 0$, which is expected for excitations produced by the continuous constrictions which has k vector smaller than constriction. Second Observation we can make is that the amplitude profile in figure (44) shows some oscillations inside the region

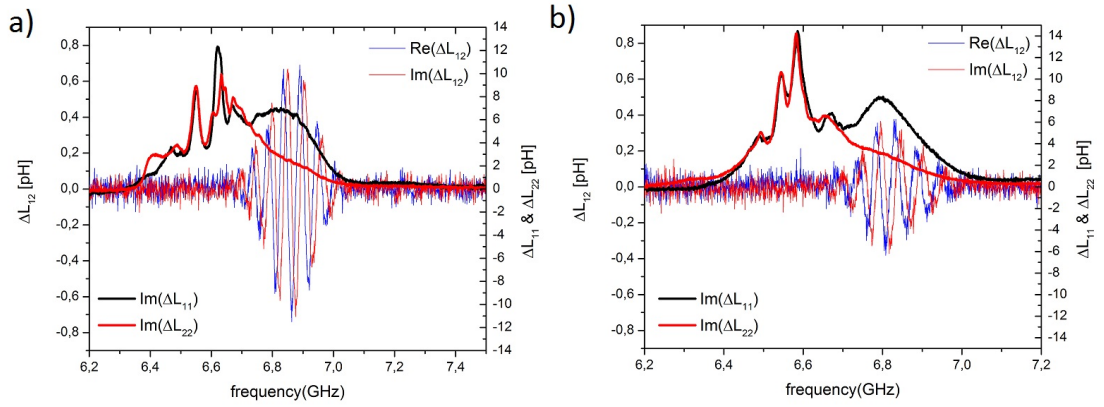

Figure 43: Spectra in Reflection both ports, and in transmission ΔL_{12} for mapping device with $\mu_o H_{ext} = 0.3741T$ a) $s = 0\mu m$ b) $s = 6\mu m$

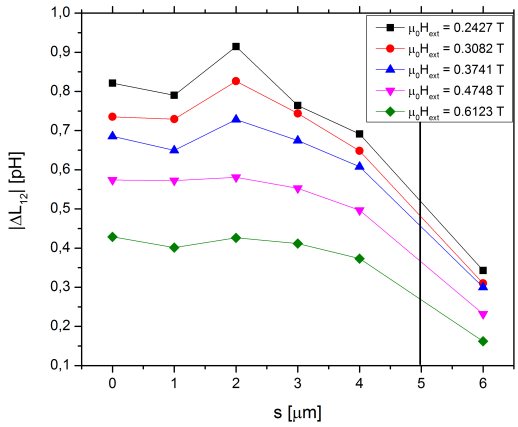

Figure 44: Mapping of amplitude for Geometry No. 1. black line shows the edge of the constriction.

of the constriction, which may show correspond to som Fresnel diffraction pattern obtained in section §(7.1).

For Geometry No. 2, we fabricated 27 mapping devices to measure amplitude of spin waves. The reason of this geometry is to have as much as possible a single CPW emitting spin waves, in a similar manner as the Fresnel simulation. The emitter has a width of $w = 10\mu m$ and the receiver $w = 2\mu m$. Emitter is placed at $D = \{4, 8, 12\}\ \mu m$ and $s = \{0, \pm 2, \pm 4, \pm 6, \pm 8\}\ \mu m$. In this case antenna is non-symmetrical we need to map in both directions, see figure (45). We measured the amplitude in transmission for each device, figure (46).

Figure (46) shows that the amplitude of spin wave decays at points outside the region of the constriction. The amplitude towards the end, positive shifts, decays to values of the order of the noise level. While points towards the bend (negative shifts) do not go to zero. This is caused by emission of the ”elbow” which radiates in this 90 degree region spanned. Secondly, we also

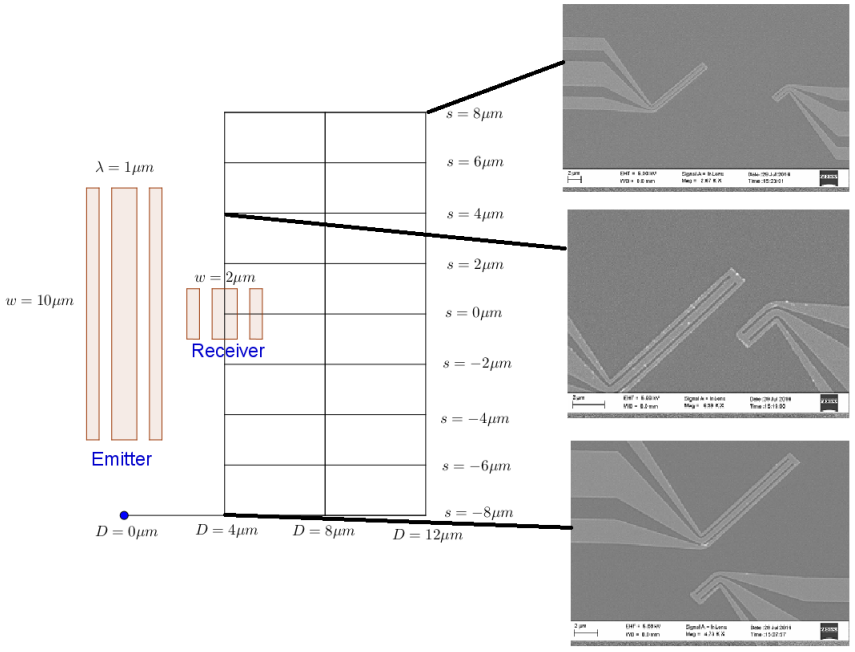

Figure 45: Mapping grid for Geometry No. 2.

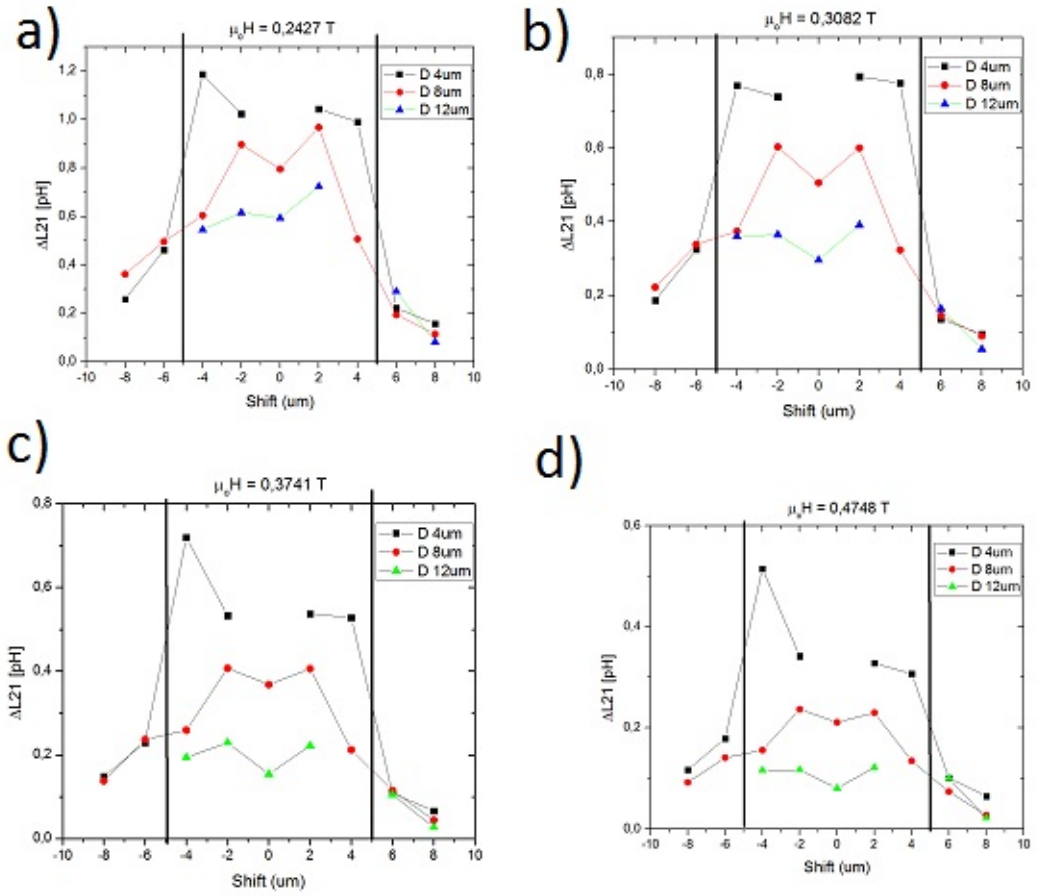

Figure 46: Mapping for Geometry No. 2. Black lines show edges of the constriction.

observed oscillations in the amplitude when the receiver is within the width of the emitter, very similar to the results of the simulations of near-field diffraction pattern we obtained in section §(7.1). Finer mapping with an smaller probe, should be done in order to confirm such a pattern. A useful technique to measure the amplitude profile of spin waves is Brillouin Light Scattering (BLS), which with the use of a laser is possible to map the amplitude of the magnetization at each point of the film. The advantages that presents this technique are that they excite single modes at a constant frequency and field, and there is no need of a pair of antennae, just one is enough.

8.4 Sudden constriction geometries

We measure the spectra in transmission for the few devices we fabricated for geometries No. 3 and No. 4 which are characterized by the perpendicular constriction. The purpose of having this type of geometries is to minimise the cross talk between the continuous constriction and the antennae as observed for geometries No. 1 and No. 2. From spectra shown in figure (47) . Geometry No. 3 shows a clear separation between the transmission between the constriction of each antenna, at larger frequency, and the larger portion of the device (peak to the left of the spectra). This assures that there is no cross talk between portion of the antenna with distinct k vector. From figure (48), the spectra corresponding to geometry No. 4 does not show cross talk, since the bigger sections of the antennae are shifted by the width of the constriction.

Unfortunately, due to some equipment breakdown toward the end of our term at IPCMS, we were not able to further study of spin wave mapping with this geometry. It appears as a geometry of choice, additional devices should be prepared to study the spin wave emission from this constriction

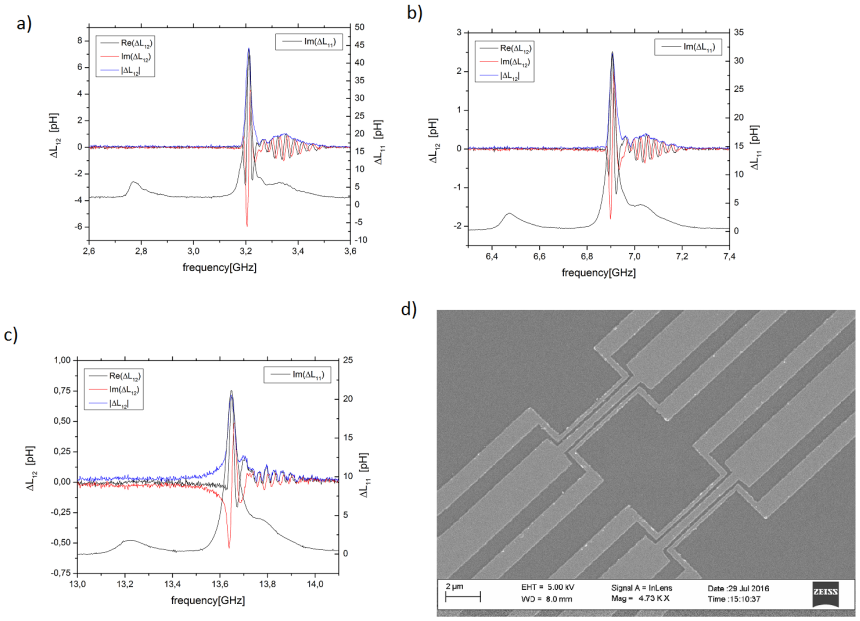

Figure 47: Spectra in transmission and reflection for Geometry No. 3 a)$\mu_o H_{ext} = 0.2427T$ b) $\mu_o H_{ext} = 0.3741T$ c) $\mu_o H_{ext} = 0.6123T$ d) SEM picture of device with $\lambda = 1\mu m$, $w = 5\mu m$, $D = 8\mu m$

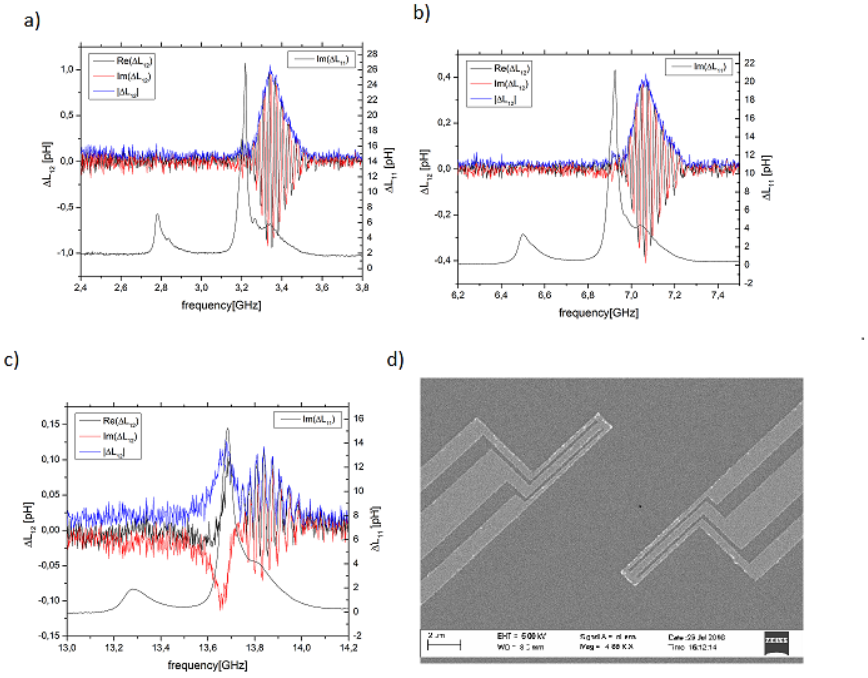

Figure 48: Spectra in transmission and reflection for Geometry No. 4 a)$\mu_o H_{ext} = 0.2427T$ b) $\mu_o H_{ext} = 0.3741T$ c) $\mu_o H_{ext} = 0.6123T$ d) SEM picture of device with $\lambda = 1\mu m$, $w = 5\mu m$, $D = 8\mu m$

9 Conclusions

Broadband Ferromagnetic resonance (FMR) in thin films is a powerful technique to characterize static and dynamic properties. When this technique is further improved combining wave guides of different size, the spectroscopic information resolved form the different k-vector allows, in particular, to distinguish the saturation magnetization (M_s) form the anisotropic field (H_k). In the present thesis, we first developed a broadband FMR setup at the USFQ implementing frequency modulation of the microwave signal, detected via diode and lock-in amplification. Using this technique we characterized thin films of YIG, 29 nm thickness, that were grown at Argonne National Laboratory. We found an effective magnetization of $\mu_o M_{eff} = 0,1405T$, gyromagnetic ratio $\gamma = 28,28GHz/T$, and intrinsic damping of $\alpha = 1.657 \times 10^{-3}$ with inhomogeneous broadening $\Delta H_o = 4,36 \times 10^{-4}T$. Currently, this setup allows to perform FMR in a field range up to $0,170[T]$ which restricted the frequency range, to typically $7GHz$ for YIG with $M_s = 0,15T$. The addition of a robust, $1.5kW$ power supply would allow with the available microwave source to perform FMR for YIG, in a frequency ranging up to $20GHz$. Also, field modulating the static field instead of the microwave signal could improve the sensitivity of our lock-in detection.

Then, we used these YIG films to study emission of a spin wave beam in a continuous layer. Based on a simple study of the Fresnel near field diffraction pattern, we identified four different potential geometries for our problem. Using the nanofabrication facility available at the *Institut de Physique et Chimie des Materiaux de Strasbourg* (IPCMS), we fabricated several series of pair of coplanar wave guide (CPW) antennae with a constriction. For two of the selected geometry, we were able to characterize, using the propagating spin wave spectrometer of the IPCMS, the attenuation length of the magnetostatic forward volume wave (MSFVW), and also measure the degree of focusing of the spin wave beam via a discrete mapping of the spin wave amplitude. For both geometries, when the two antennae were completely shifted, we observed a drastic decrease of the spin wave amplitude outside of the region of the constriction which suggests a relatively well focused spin wave beam. However a residual transmission signal still remained due to crosstalk between the constricted section of the CPW and the rest of the CPW. In particular, it appears difficult to avoid such a crosstalk with a continuous constriction such as the one of geometry No.1, which excite a broad range of k-vectors that can be detected by the smaller section of the second antennae. In order to suppress this cross talk, we found that a sudden constriction, such as geometry No.3, is a better candidate, since each of the section of the CPW have well separated resonant peaks. Finally, the spectra of the mapping devices for shift smaller than the length of the constriction showed some oscillations of the spin wave amplitude very similar to the Fresnel diffraction pattern obtained in our simulations. Brillouin light scattering measurements of the four different geometries of antennae for the magnetostatic surface wave mode are under way at Argonne National Laboratory. This optical technique

should offer a finer spatial resolution of the confinement of the spin wave beam for each type of constriction, as well as any possible diffraction pattern.

Further investigations of optimum geometry remain to evidence a sharp focused spin wave beam. The possibility of generating a spin wave beam in a continuous ferromagnetic layer offers the perspective to study the interference patterns between two or more interacting spin wave beams. This will undoubtedly contribute to further insights for potential magnonic applications.

Appendices

Appendix A: High Frequency Basics: Propagation of EM waves in transmission lines

Transmission lines are studied in order to obtain solutions for the current and voltage in a transmission line. Normally a line is composed in two conductors that conduct current in opposite directions, and a dielectric between them, we can think on two wires separated by a distance or a coaxial line, that we will study later. Special transmission lines are those which supports the propagation of Transverse Electric Magnetic (TEM) modes, wave guides where the component of the $\mathbf{E}$ and $\mathbf{B}$ field are zero in the direction of propagation and orthogonal to each other. This kind of transmission lines are important because it allows to define the current in the conductors and voltage between them. A transmission line is characterized by four parameters, the losses in conduction given by a resistance in series R, the reactive losses in energy given by an inductance L in series with R. Also, by the conductance of the dielectric G, that represents the losses due to conduction between conductors, and the reactive losses in energy due to the capacitance C between conductors. We can see a transmission line as shown in figure (49), which represents a differential section dx of a line.

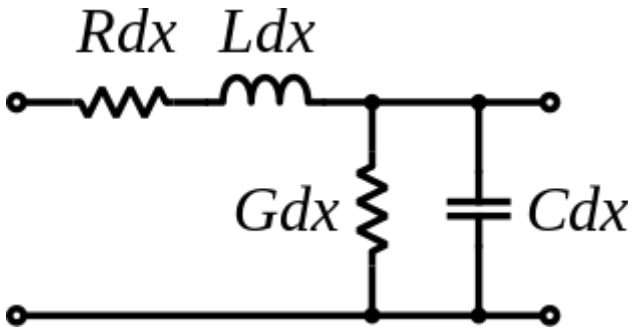

Figure 49: Differential section of a transmission line

Writing the fall of potential and current at the end of this differential section of the transmission line we obtain:

$$dV = -\left(IRdx + L\frac{\partial I}{\partial t}dx\right) \tag{123}$$

$$dI = -\left(GVdx + C\frac{\partial V}{\partial t}dx\right) \tag{124}$$

We can rewrite the following equations as a system of coupled equations for I and V:

$$\frac{\partial V}{\partial x} = -IR - L\frac{\partial I}{\partial t} \tag{125}$$

$$\frac{\partial I}{\partial x} = -GV - C\frac{\partial V}{\partial t} \tag{126}$$

Lets suppose answers of the form

$$I(x,t) = Re\{\tilde{I}(x)e^{i\omega t}\} \qquad V(x,t) = Re\{\tilde{V}(x)e^{i\omega t}\} \tag{127}$$

we separate spatial and temporal dependence, so we obtain equations just for the spatial dependence:

$$\frac{\partial \tilde{V}}{\partial x} = -\tilde{I}R - i\omega L\tilde{I} \tag{128}$$

$$\frac{\partial \tilde{I}}{\partial x} = -G\tilde{V} - i\omega C\tilde{V} \tag{129}$$

We obtain the following equations

$$\frac{\partial^2 \tilde{V}}{\partial x^2} = \gamma^2 \tilde{I} \qquad \frac{\partial^2 \tilde{V}}{\partial x^2} \tag{130}$$

where

$$\gamma^2 = (G + i\omega C)(R + i\omega L) \tag{131}$$

This two equations has solutions of the form:

$$\tilde{V}(x) = V_+ e^{\gamma x} + V_- e^{-\gamma x} \tag{132}$$

$$\tilde{I}(x) = I_+ e^{\gamma x} + I_- e^{-\gamma x} \tag{133}$$

Solutions, as expected is a linear combination of travelling waves in both directions. Now, we can define given these free parameters, the *characteristic impedance* at any point of the line given by:

$$Z_c = \frac{V_+}{I_+} = -\frac{V_-}{I_-} = \sqrt{\frac{R + i\omega L}{G + i\omega C}} \tag{134}$$

we find last expression using equations (128) and (129). Both γ and Z_c are complex numbers, therefore we can define $\gamma = \sigma + i\beta$, where σ is the attenuation factor and β is the phase factor. We can write the complete solution for $V(x,t)$:

$$V(x,t) = \tilde{V}_+ e^{-\sigma} e^{i(\omega t - \beta x)} \tag{135}$$

From this equation we can define the phase velocity of the wave as:

$$v_{ph} = \frac{\omega}{\beta} \tag{136}$$

For low lose transmission lines we have that, $R \ll \omega L$ and $G \ll \omega C$, we can approximate v_{ph} and Z_c as follows:

$$v_{ph} \approx \frac{1}{\sqrt{LC}} \qquad Z_c \approx \sqrt{\frac{L}{C}} \tag{137}$$

Historically, transmission lines are built with $Z_c = 50\Omega$. This impedance is the balance between high break voltage and low losses for radiation. In general, transmission lines in any instrument used on the transmission and detection of microwaves should have impedance of 50Ω in order to avoid losses of signal due to reflection[1].

Appendix B: Coaxial line

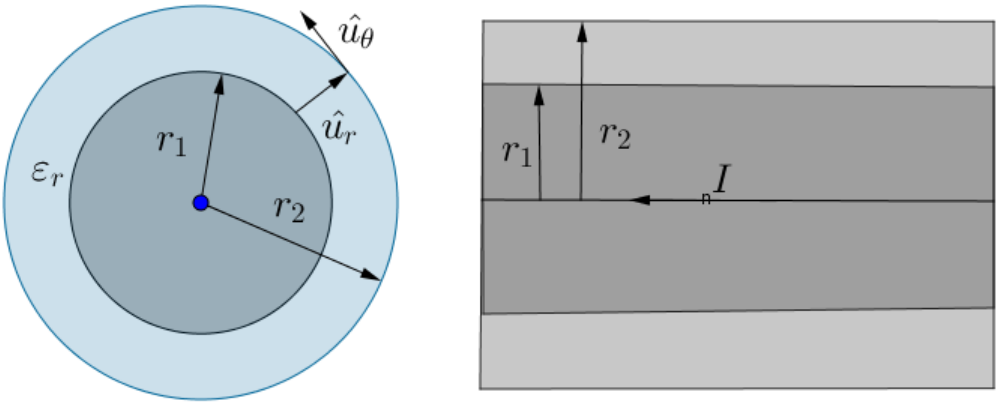

Figure 50: Coaxial transmission line

Coaxial transmission line are two concentric cylindrical conductors, and a dielectric material between them, as shown in figure 50. This geometry supports the transmission of TEM modes because, $\mathbf{E}$ and $\mathbf{B}$ are perpendicular between them and to the propagation direction. Using Ampere's law we can calculate the magnetic field.

$$\mathbf{B} = \mu_o \frac{I}{2\pi r} \hat{u_\theta} \tag{138}$$

the magnetic flux trough a strip of width dz is given by:

$$\phi = \mu_o \frac{Idz}{2\pi} \int_{r_1}^{r_2} \frac{dr}{r} = \mu_o \frac{Idz}{2\pi} \ln\left(\frac{r_2}{r_1}\right) \tag{139}$$

Therefore, the inductance per unit length of the line is:

$$L = \frac{\phi}{Idz} = \frac{\mu_o}{2\pi} \ln\left(\frac{r_2}{r_1}\right) \tag{140}$$

Using Gauss' law we can calculate the $\mathbf{E}$ field between the conductors:

$$\mathbf{E} = \frac{\lambda}{2\pi\epsilon r} \hat{u_r} \tag{141}$$

where λ is the charge per unit length of the conductor, and $\epsilon = \epsilon_r \epsilon_o$ is the permittivity of the dielectric. Now we can calculate voltage between conductors:

$$V = \frac{\lambda}{2\pi\epsilon} \int_{r_1}^{r_2} \frac{dr}{r} = \frac{\lambda}{2\pi\epsilon} \ln\left(\frac{r_2}{r_1}\right) \tag{142}$$

then the capacitance is:

$$C = \frac{Q}{V} = \epsilon \frac{2\pi}{\ln\left(\frac{r_2}{r_1}\right)} \tag{143}$$

With the expressions for L and C, we can calculate the phase velocity and characteristic impedance of a coaxial cable.

$$v = \frac{1}{\sqrt{\varepsilon\mu_o}} \qquad Z_c = \frac{1}{2\pi}\sqrt{\frac{\mu_o}{\varepsilon}} \ln\left(\frac{r_2}{r_1}\right) \tag{144}$$

As mentioned in the last section, the geometry of the wave guide is such it produces a 50Ω impedance. The use of a waveguide to measure Ferromagnetic resonance lies on the fact that the phase velocity and characteristic impedance depends on the permeability of the media. When the frequency of the wave matches with the resonance condition, the permeability changes as we determined on section §1.5.3, this will induce a change on the phase velocity which is a measurable parameter[1].

Appendix C: Electromagnet Calibration

We use the homemade electromagnet provided by the laboratory of Dr. Bailleul. We calibrate this electromagnet using a hall probe, and a Lakeshore Gaussmeter. We measure the magnetic field value as a function of the coil current. We obtained plot of figure (51), we fit this data with a third degree polynomial:

$$H_{ext}(I) = 0.0383 + 0.3582I - 0.00319I^2 - 0.00431I^3 \tag{145}$$

We also measure the field inhomogeneities as function of the distance from the center of the pole. Using the hall probe we measure the field for a fixed value of current, which then was normalized to the correspondent field value given by prior calibration, at different distances to the center of the pole. We obtained the plot in figure (52) where we can observe a drop of 3.71% of the field over $2\,mm$ from the center. We fit this data with a 6th degree polynomial, we obtained the following relation

$$H_{ext}(r)/H_{ext}(r=0) = 1.00014 - 0.00597r^2 + 0.00048032r^4 - 0.0043276r^6 \tag{146}$$

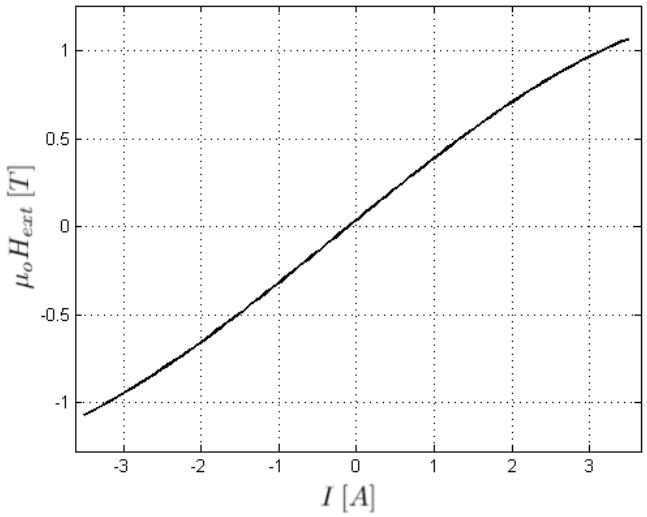

Figure 51: Plot of magnetic field in the region between the poles as a function of the coil current. $H_{ext}(I)$

We obtain the following expression which relates the magnetic field with the coil current and the distance to the center of the pole.

$$H_{ext}(I,r) = (1.00014 - 0.00597r^2 + 0.00048032r^4 - 0.00043276r^6) \\ (0.0383 + 0.3582I - 0.00319I^2 - 0.00431I^3) \tag{147}$$

Appendix D: Spin Coat details

Details to spin coat a YIG thin film with bilayer resin and conductive resin:

- Clean the sample film with ultrasonic bath in Acetone, for 5 min. After, an ultrasonic bath in Isopropanol. This step eliminate any dust particle from the film.
- Cover the film with resin, $\approx 90nm$ thickness, using Spin coating. We used Resin PMMA (Poly methyl methacrylate) ARP 619.04, spin coated at 1000 rpm.
- baked the sample to solidify the resin. Using a precision hot plate, sample was baked at $180°C$, for $1:30$ min.
- Second layer of resin PMMA ARP-679.02 spin coated at 1000 rpm.
- Bake at $180°C$ for $1:30$ min.

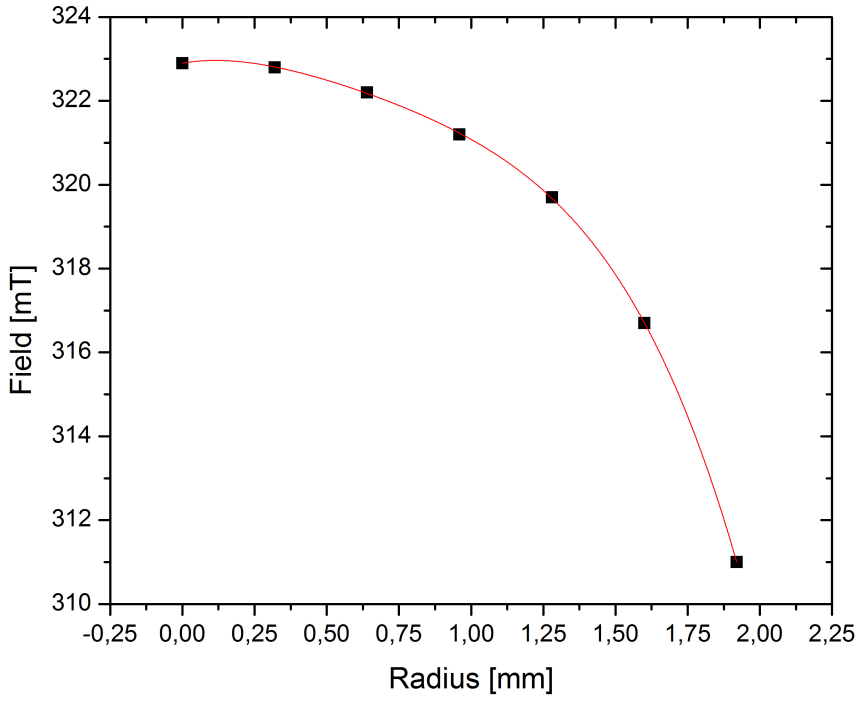

Figure 52: Field inhomogeneities of magnetic field as function of the distance to the center of the pole, for $I = 0.5\ A$

- Cover film with conductive resin (SX AR-PL 5000/90.2), thickness $35nm$, spin coated at 4000 rpm. Conductive resin is used to see under the e-beam microscope, because YIG is an electrical insulator.
- Bake at $90°C$ for 1:30 min.

10 References

References

[1] BILZER, C. *Microwave susceptibility of thin Ferromagnetic flims: metrology and insight into magnetization dynamics*, Thèse de Doctorat Université Paris-Sud 11, 2007

[2] COEY, J. M. D. *Magnetism and Magnetic Materials*, Cambridge University Press, Cambridge, UK, 2010.

[3] GUREVICH, A. G., MELKOV, G. A.,*Magnetization Oscillations and Waves*, CRC Press, Boca Raton, FL, 1996.

[4] LENK, B. ULRICHS, H. GARBS, F. MÜNZENBERG, M. *The Building Blocks of Magnonics,* Physics Reports, **507** , (2011), 107–136 .

[5] STANCIL, D., *Theory of Magnetostatic Waves*, Springer-Verlag, New York, NY, 1993.

[6] VLAMINCK, V. *Décalage Doppler d'onde de spin induit par un courant électrique*, Thèse de Doctorat de L'Université Louis Pasteur, 2008

[7] WEI, Y. *Ferromagnetic Resonance as a Probe of Magnetization Dynamics. A study of FeCo thin films and trilayers*, Uppsala Dissertations from the Faculty of Science and Technology 112. 125 pp. Uppsala: Acta Universitatis Upsaliensis, 2015.

[8] GRUSZECKI, P. KASPRZAK, M. SEREBRYANNIKOV, E. KRAWCZYK, M. ŚMIGAJ, W. , *Microwave excitation of spin wave beams in thin ferromagnetic films*, Science, Sceintific Reports, 2016.

[9] VLAMINCK, V. BAILLEUL, M *Spin-Wave transduction model at submicrometer scale.*, Physical REview B, **81**, 014425(2010).

[10] STIGLOHER, G. DECKER, M. KORNER, H.S. TANABE, K. MORIYAMA, T. TAMIGICHI, T. HATA, H. MADAMI, M. GUBBIOTTI,

G. KOBAYASHI, K. ONO, T. BACK, C.H. *Snell's Law for Spin Waves.*, Physical Review Letter, accepeted.

[11] HECHT, E. *Optics.*, Addison Wesley, San Francisco, CA. 4th Ed.

[12] KRUGLYAK, V. DEMOKRITOV, S. GRUNDLER, D. *Magnonics.*, Journal of Physics D: Applied Letters, accepeted. **43**, (2010)264001

[13] KHITUN, A. BAO,M. WANG, J. D., Phys. D: Appl. Phys. **43**, 264005 (2010)

[14] KOSTYLEV, M. SERGA, Q. SCHNEIDER, T. LEVEN, B. HILLERBRANDS, B. *Spin-Wave logical gates*, Appl. Phys. Letters. **87**, 153501 (2005)

[15] SCHNEIDER, T. SERGA, Q. LEVEN, B. HILLERBRANDS, B. KOSTYLEV, STAMPS, R. M. *Realization of spin-Wave logic gates*, Appl. Phys. Letters. **92**, 022505 (2008)

[16] MONTOYA, E. McKINNON, T. ZAMANI, A. GIRT, E. HEINRICH, B. *Broadband ferromagnetic resonance system and methods for ultrathin magnetic fileds.*, Physical Review B, **81**, 014425(2010).